Title: ARID1A governs the silencing of sex-linked transcription during male meiosis in the mouse

Debashish U. Menon, Prabuddha Chakraborty, Noel Murcia, & Terry Magnuson*

Department of Genetics, and Lineberger Comprehensive Cancer Center, The University of North Carolina at Chapel Hill, Chapel Hill, NC 27599-7264, USA

*Correspondence: trm4@med.unc.edu, Tel 919-357-2924, Fax 919-843-4682

Abstract

We present evidence implicating the BAF (BRG1/BRM Associated Factor) chromatin remodeler in meiotic sex chromosome inactivation (MSCI). By immunofluorescence (IF), the putative BAF DNA binding subunit, ARID1A (AT-rich Interaction Domain 1a), appeared enriched on the male sex chromosomes during diplonema of meiosis I. The germ cell-specific depletion of ARID1A resulted in a pachynema arrest and failure to repress sex-linked genes, indicating a defective MSCI. Consistent with this defect, mutant sex chromosomes displayed an abnormal presence of elongating RNA polymerase II coupled with an overall increase in chromatin accessibility detectable by ATAC-seq. By investigating potential mechanisms underlying these anomalies, we identified a role for ARID1A in promoting the preferential enrichment of the histone variant, H3.3, on the sex chromosomes, a known hallmark of MSCI. Without ARID1A, the sex chromosomes appeared depleted of H3.3 at levels resembling autosomes. Higher resolution analyses by CUT&RUN revealed shifts in sex-linked H3.3 associations from discrete intergenic sites and broader gene-body domains to promoters in response to the loss of ARID1A. Several sex-linked sites displayed ectopic H3.3 occupancy that did not co-localize with DMC1 (DNA Meiotic Recombinase 1). This observation suggests a requirement for ARID1A in DMC1 localization to the asynapsed sex chromatids. We conclude that ARID1A-directed H3.3 localization influences meiotic sex chromosome gene regulation and DNA repair.

Introduction

Meiosis is central to the formation of haploid gametes from diploid progenitors. During meiosis, homologous chromosomes pair, exchange genetic material, align at the metaphase plate, and then segregate during the first meiotic cell division. Unlike autosomal homologs, the X and Y chromosomes share limited homology. Unique mechanisms have evolved to ensure these chromosomes become sequestered and processed in a parallel but distinct process from autosomes.

XY chromosomes pair along the pseudo-autosomal region (PAR), leaving extensive regions of the X and Y unpaired. These regions become enriched for DNA damage response (DDR) factors, including ATR (Ataxia Telangiectasia and Rad3 related), TOPBP1 (DNA topoisomerase II-binding protein 1), and MDC1 (Mediator of DNA Damage Checkpoint 1), which amplifies γH2A.X across XY chromatin (Alavattam et al., 2022; ElInati et al., 2017; Fernandez-Capetillo et al., 2003; Ichijima et al., 2011; Royo et al., 2013; Turner et al., 2004). XY chromatin acquires further distinguishing features when the variant histone H3.3 replaces the canonical histones H3.1/3.2, and H3K9me3 (Histone lysine9 trimethylation) becomes elevated on XY chromatin relative to autosomes (Hirota et al., 2018; van der Heijden et al., 2007; Yuen et al., 2014). As the XY chromosomes become epigenetically distinct from autosomes, they also become physically separated into a unique nuclear sub-compartment known as the XY body (Handel, 2004). Transcriptional silencing of unpaired chromatin occurs during this phase of meiosis I, known as meiotic silencing of unpaired chromatin (MSUC) (Turner, 2007). MSUC of autosomal chromatin, such as in response to an abnormal karyotype, causes pachynema arrest and cell death (Baarends et al., 2005; Schimenti, 2005; Turner et al., 2005). However, silencing unpaired XY chromatin results in a different outcome known as meiotic sex chromosome inactivation (MSCI) (Alavattam et al., 2022). Sex chromosomes are required to undergo MSCI and become transcriptionally inactivated. Failure to achieve MSCI triggers arrest and cell death (Ichijima et al., 2011).

Chromatin factors that influence MSCI include the H3K9 methyltransferase, SETDB1 (SET domain, bifurcated 1), PRC1 associated SCML2 (Sex comb on midleg-like protein 2), and testis-specific reader of histone acetylation, BRDT (Bromodomain testis-specific protein) (Hasegawa et al., 2015; Hirota et al., 2018; Manterola et al., 2018). Previous studies demonstrated a critical requirement for SWI/SNF-directed transcriptional regulation during meiosis (Kim et al., 2012; Menon et al., 2019; Wang et al., 2012). The germ cell-specific depletion of the SWI/SNF catalytic subunit, BRG1(Brahma-related gene-1), resulted in an early pachytene arrest (Kim et

al., 2012). BRG1 is associated with the XY body (Wang et al., 2012), but its requirement for MSCI is unknown. This lack of evidence for MSCI is also true for the PBAF (POLYBROMO1-BRG1/BRM Associated Factor) remodeler within the SWI/SNF family, which we have shown is required for meiotic cell division (Menon et al., 2021). Whether these data suggest a role for PBAF in MSCI remains an open question, given that BRG1 associates with both SWI/SNF remodelers, PBAF and BAF.

Here, we find that ARID1A (AT-rich Interaction Domain 1a), a BAF-specific putative DNA binding subunit, is required for the transcriptional silencing of the sex chromosomes during pachynema, thereby ensuring meiotic progression through prophase-I. Mechanistically, ARID1A is necessary to establish MSCI hallmarks, such as the eviction of elongating RNA polymerase-II (phosphorylated on Serine2 of carboxy-terminal domain; pSer2-RNAPII), limited sex-linked chromatin accessibility, and hyper-accumulation of histone H3.3 on the sex body. Additionally, ARID1A is required for the targeted localization of DMC1 to the unpaired sex chromatids, implicating BAF-A-governed sex-linked chromatin dynamics in DNA repair.

Results

Meiotic progression requires ARID1A

Meiotic progression in male mice depends on SWI/SNF-regulated gene expression (Menon et al., 2019; Menon et al., 2021). These studies raise the prospect of distinct SWI/SNF subcomplexes governing stage-specific meiotic transcription (Menon et al., 2021). To understand the meiotic functions of the biochemically distinct SWI/SNF BAF subcomplex, we examined the spermatogenic expression profiles of the BAF subunits *Arid1a* and *Arid1b* using single-cell RNA-seq data generated from testes (Ernst et al., 2019). *Arid1a* mRNA expression occurred at various spermatogenic stages with notable expression at pachynema of meiotic prophase I (Fig. S1A-C).

Arid1b mRNA went undetectable until late in spermiogenesis (Fig. S1A, D-E). Consistent with its mRNA expression profile, pachytene spermatocytes featured abundant ARID1A protein, which was uniformly spread among autosomes and sex chromosomes (Fig. 1). Late in diplonema, ARID1A appeared preferentially enriched on the sex chromosomes as compared to autosomes (Fig. 1). These data implicate ARID1A in meiotic sex chromosome inactivation (MSCI), a process essential for meiotic progression in males.

To determine whether meiotic spermatocytes require ARID1A, we generated a germ cell-specific knock-out of *Arid1a* using the *Stra8-Cre* transgene expressed in spermatogonia (Sadate-Ngatchou et al., 2008). *Stra8-Cre* was chosen among the available germ-cell-specific Cre lines to circumvent *Arid1a* haploinsufficiency during embryonic development. *Stra8-Cre* remains inactive during embryonic development when transmitted through females (Sadate-Ngatchou et al., 2008). The number of undifferentiated spermatogonia that stained positive for Promyelocytic leukemia zinc finger (PLZF^{+}, also known as Zinc finger and BTB domain containing 16: ZBTB16) remained unchanged in *Arid1a*^{cKO} testes (Table S1). The proportions of undifferentiated spermatogonia (PLZF+) with detectable (ARID1A+) and non-detectable (ARID1A-) levels of ARID1A protein determined by immunostaining on testes cryosections obtained from 1-month old *Arid1a*$^{fl/fl}$ (control) and *Arid1a*^{cKO} (CKO) males was 74% ARID1A^{-} (CKO, n = 179) and 26% ARID1A^{+} (CKO, n = 65) as compared to 95% ARID1A^{+} (n = 88) and 5% ARID1A^{-} (n = 5) in controls. Western blot analysis also showed a significant reduction in ARID1A protein in mutant pachytene spermatocytes (Fig. S2). Therefore, the *Arid1a* conditional knockouts generated with a *Stra8-Cre* did not appear to impact earlier stages of spermatogenesis. Potential defects early in spermatogenesis might occur with an earlier-acting germline Cre transgene. In this case, an inducible Cre transgene would be needed, given the haploinsufficiency associated with *Arid1a*.

Contrary to our expectations, meiosis appeared unperturbed, as evidenced by seminiferous tubules featuring round and elongated spermatids in *Arid1a*^{cKO} testes (Fig. S3A). Furthermore, *Arid1a*^{cKO} epididymis featured mature spermatozoa, suggesting that *Arid1a*^{cKO} testes are capable of normal spermatogenesis (Fig. S3B). Although these data indicate that ARID1A is dispensable for spermatogenesis, we wanted to confirm that these results were not a technical artifact arising from inefficient *Stra8-Cre* mediated excision of the *Arid1a*^{fl} allele.

To address this question, we examined *Arid1a* transcripts isolated from *Arid1a*^{WT} and *Arid1a*^{cKO} Sta-Put purified populations of pachytene spermatocytes and round spermatids using RT-PCR (Fig. S4A). For cDNA synthesis, we used primers that amplify a 612 bp region spanning the *Arid1a* floxed exons 5 and 6. Assuming 100% CRE efficiency, we would expect to observe a 281 bp cDNA product associated with mRNA isolated from *Arid1a*^{cKO} spermatogenic cells. Instead, we observed cDNAs representative of the floxed (*fl*) allele and, to a greater extent, the excised (Δ) allele from mRNA isolated from *Arid1a*^{cKO} pachytene spermatocytes. These results

indicated inefficient CRE activity (Fig. S4A). More importantly, the data suggest that a fraction of pachytene spermatocytes in *Arid1a*^{cKO} testes fail to undergo CRE-mediated excision, resulting in escapers. An examination of ARID1A levels in testes cryosections and meiotic spreads by immunofluorescence (IF) revealed a heterogenous population of pachytene spermatocytes consisting of mutants lacking and escapers expressing ARID1A (Fig. S4B, C). On average, 70% of pachytene spermatocytes were observed lacking detectable levels of ARID1A signal by IF.

Furthermore, examining the meiotic profile associated with *Arid1a*^{cKO} revealed an accumulation of mutant spermatocytes (ARID1A^{-}), some at leptonema and zygonema and a majority at mid-pachynema relative to *Arid1a*^{WT} spermatocyte spreads (Table 1). Some diplotene spermatocytes displaying a moderate reduction in ARID1A levels occurred in *Arid1a*^{cKO} relative to *Arid1a*^{WT} meiotic spreads and represent escapers due to inefficient *Stra8-Cre* activity (Table 1 - bottom two lines with asterisks, also Fig. S4B,C). However, diplotene and metaphase-I spermatocytes lacking ARID1A protein by IF were undetectable in the *Arid1a*^{cKO} testes (Fig. S4B). These results indicate a mid-pachytene arrest in the mutant spermatocytes. The spermatocytes that escape Cre activity progress to subsequent meiotic stages, giving rise to genotypically normal gametes. All round spermatids isolated from *Arid1a*^{cKO} testes appeared only to express the normal transcript associated with the floxed allele (Fig. S4A). Therefore, the perceived lack of a phenotype is an artifact of inefficient *Stra8-Cre* inefficiency. But more importantly, the data indicate that ARID1A is essential for progression beyond pachynema.

ARID1A regulates the transcriptional silencing of the sex chromosomes at pachynema

The meiotic requirement of ARID1A and, more importantly, its association with the sex chromosomes at diplonema prompted us to examine its role in MSCI. We hypothesized that ARID1A might play a role in the transcriptional silencing of the sex-linked genes during meiosis. To address this question, we performed RNA-seq on Sta-Put purified populations of pachytene spermatocytes to profile changes in transcript abundance upon ARID1A deficiency. Differential analysis of gene expression using DeSeq2 (Love et al., 2014) revealed an equal proportion of significantly (FDR < 0.05) misexpressed genes displaying either elevated (up-regulated, n= 5824) or reduced (down-regulated, n=5821) transcript abundance in *Arid1a*^{cKO} relative to *Arid1a*^{WT} pachytene spermatocytes (Fig. 2A). Notably, we detected significant misexpression of 53% of all the sex-linked coding genes (593/1105) in response to an ARID1A deficiency. Amongst these, 86.4% displayed elevated expression (n=512), whereas only 13.6% displayed reduced (n=81) transcript abundance. This skew was even greater when only considering sex-

linked genes misexpressed by a magnitude of 2 LOG-fold or higher. Here, 97% (297/306) of the misexpressed sex-linked genes displayed increased transcript abundance in response to an ARID1A deficiency. Therefore, ARID1A predominantly affects the repression of sex-linked genes during pachynema.

An examination of changes in the average transcript abundance on a chromosome-wide basis showed that expression from the sex chromosomes was significantly higher than that from autosomes in response to the loss of ARID1A at pachynema (Fig. 2B). Therefore, ARID1A regulates the transcriptional repression of the sex chromosomes, implicating it in MSCI. ARID1A's influence on sex-linked gene regulation may result from its association with the sex chromosomes, particularly during diplonema, where ARID1A hyper-accumulates on the XY. However, during pachynema, when MSCI initiates, ARID1A associates with the XY at autosomal levels as detected by IF (Fig. 1). Therefore, it is possible that, at the onset of pachynema, local ARID1A association rather than chromosome-wide coating dictates its role in sex-linked gene repression.

To address ARID1A's association with the XY chromosomes, we determined its genomic localization at a higher resolution by CUT&RUN (Cleavage Under Targets & Release Using Nuclease) in pachytene spermatocytes. We detected ARID1A occupancy at promoters of differentially regulated target genes, irrespective of their chromosomal location, in *Arid1a*^{WT} relative to *Arid1a*^{cKO} (negative control) pachytene spermatocytes (Fig. S5). This result is consistent with the genome-wide distribution of ARID1A observed in pachytene spermatocyte spreads by IF (Fig. 1). Although not detectable by IF, pachytene spermatocytes displayed a preferential association of ARID1A with promoters of normally repressed sex-linked genes, when detected by CUT&RUN (Fig. S5B), emphasizing its role in MSCI.

ARID1A does not influence DNA damage response signaling on the sex body

Unlike autosomal homologs that complete pairing during pachynema, the non-homologous regions of the sex chromosomes feature unrepaired DNA double-strand breaks (DSBs). These DNA DSBs recruit γH2Ax, a product of DNA damage response (DDR) signaling pathways essential for establishing and maintaining MSCI (Turner, 2007). Therefore, to determine whether ARID1A regulated MSCI by influencing DDR signaling, we first monitored the association of γH2Ax with the sex chromosomes in response to the loss of ARID1A. By IF, γH2Ax accumulation on the sex body appeared unperturbed in the mutant (ARID1A^{-}) relative to

escapers (ARID1A^{+}) and *Arid1a*^{WT} pachytene spermatocytes (Fig. S6A). Consistent with this, the recruitment of ATR (Ataxia Telangiectasia and Rad3 related), a kinase known to phosphorylate γH2Ax and initiate MSCI (Royo et al., 2013; Turner et al., 2004), appeared normal in the absence of ARID1A. These data indicate that sex-linked DDR signaling occurred independently of ARID1A (Fig. S6B). As expected, MDC1 (Mediator of DNA damage Checkpoint 1), a known γH2Ax reader that is essential for sex body formation (Ichijima et al., 2011), remained associated with the asynapsed sex chromosomes upon ARID1A deletion during pachynema (Fig. S6C). These data show that the mechanisms underlying ARID1A-mediated repression of the sex-linked transcription are mutually exclusive to DDR pathways regulating sex body formation.

ARID1A limits RNAPII localization to the sex chromosomes during pachynema

Apart from γH2Ax, the association of the sex chromosomes with RNA polymerase II (RNAPII) distinguishes the sex body from the autosomes during pachynema. Normally, pachytene spermatocytes display reduced levels of RNAPII on the sex body relative to autosomes (Khalil et al., 2004). This sub-nuclear localization of RNAPII coincides with increased transcriptional output, which peaks at diplonema (Ernst et al., 2019), underscoring the importance of targeted mechanisms regulating sex chromosome repression. Therefore, we were curious to test whether ARID1A influenced the nuclear localization of RNAPII during pachynema. We performed IF to monitor the localization of the actively transcribing (elongating) form of RNAPII marked by Serine2 phosphorylation (pSer2) on its carboxy-terminal domain (Noe Gonzalez et al., 2021). We monitored elongating RNAPII (pSer2) because its pausing regulates meiotic transcription (Alexander et al., 2022). By co-staining for RNAPII (pSer2) and SYCP3, we could stage pachynema and identify the sex chromosomes. While RNAPII (pSer2) localization to the autosomes appeared similar, we noticed increased levels of RNAPII (pSer2) association with the sex chromosomes in *Arid1a*^{cKO} relative to *Arid1a*^{WT} mid and late pachytene spermatocytes (Fig. 3A). By quantifying the RNAPII (pSer2) signal generated by IF, we detected a 1.5-fold increase ($p=0.0003$) in the average RNAPII (pSer2) fluorescence associated with the sex chromosomes in *Arid1a*^{cKO} relative to *Arid1a*^{WT} pachytene spermatocytes (Fig. 3B).

Due to technical difficulties, we could not simultaneously stain for ARID1A alongside SYCP3 and RNAPII (pSer2), making distinguishing escapers from mutants in the *Arid1a*^{cKO} meiotic spreads impossible. This result suggests that the 1.5-fold increase in RNAPII association with the sex body in *Arid1a*^{cKO} relative to *Arid1a*^{WT} pachytene spermatocytes is likely underestimated.

Therefore, our results indicate that ARID1A facilitates sex-linked gene repression by limiting the association of elongating RNAPII with the sex chromosomes during pachynema.

ARID1A regulates promoter accessibility during pachynema

Next, we hypothesized that ARID1A-governed chromatin remodeling might underlie its role in limiting RNAPII accessibility on pachytene sex chromosomes. Therefore, we profiled changes in chromatin accessibility in response to the loss of ARID1A using ATAC-seq. Normally, ATAC-seq peaks (accessible chromatin) are mapped comparably across promoters (34%), intergenic (22.8%), and intronic (21.5%) regions. In contrast, the loss of ARID1A resulted in a dramatic shift towards predominantly promoter-associated ATAC-seq peaks with only a minority mapping to intergenic and intronic regions (Fig. 4A).

Consistent with an increase in the proportion of promoter-associated peaks, we detected an increase in accessibility across transcription start sites (TSS) associated with both autosomal and sex-linked differentially expressed genes (DEG's) in *Arid1a*^{cKO} relative to *Arid1a*^{WT} pachytene spermatocytes (Fig. 4B,C). Furthermore, in the case of autosomal targets, chromatin accessibility at their TSSs was enhanced irrespective of their transcriptional status, appearing indistinguishable between down-regulated and up-regulated genes upon the loss of ARID1A (Fig. 4B). In contrast, on the sex chromosomes, the loss of ARID1A seemed to have a prominent effect on TSS's associated with up-regulated genes, which displayed greater chromatin accessibility relative to their down-regulated counterparts (Fig. 4C). Therefore, the increased promoter accessibility of normally repressed sex-linked genes may underlie their persistent transcription by RNAPII upon the loss of ARID1A. Overall, these data highlight a role for BAF complexes in limiting promoter accessibility, especially on the sex chromosomes during pachynema.

ARID1A regulates the chromatin composition of the sex body

Chromatin remodelers regulate DNA accessibility by altering nucleosome positioning or composition (Clapier et al., 2017). The latter outcome is interesting in the context of MSCI, given that the sex body typically displays a striking enrichment of the variant histone H3.3 while concomitantly appearing depleted of the canonical histones H3.1/3.2 (van der Heijden et al., 2007; Yuen et al., 2014). Given that human ARID1A regulates H3.3 genomic associations (Reske et al., 2022), we tested whether a similar mechanism governed H3.3 localization to the sex chromosomes. To address this, we monitored H3.3 localization in pachytene spermatocytes

by IF, simultaneously staining for ARID1A and HORMAD1. The former aided in mutant identification, while the latter labeled the pachytene sex chromosomes. Consistent with previous reports, H3.3 preferentially coats the sex chromosomes, distinguishing it from autosomal chromatin during normal pachynema (Fig. 5A). Interestingly, this sex-body association of H3.3 was detected less frequently early in pachynema (17%), becoming more pervasive during the mid (70 %) and late (95%) stages of pachynema. In contrast, in the absence of ARID1A, H3.3 staining on the sex chromosomes was indistinguishable from their autosomal counterparts throughout pachynema (Fig. 5A). Notably, the majority of mutant mid (89%) and late (77%) pachytene spermatocytes lacked the typical sex body enrichment of H3.3 (Fig. 5A), indicating that ARID1A dictates the preferential accumulation of H3.3 on the sex body.

Next, we were curious to know the consequence of reduced H3.3 association on H3.1/3.2 occupancy on the sex body in response to the loss of ARID1A. We performed IF to monitor the association of H3.1/3.2 with the sex chromosomes marked by HORMAD1 in response to the loss of ARID1A. Like H3.3, canonical H3.1/3.2 appeared uniformly distributed genome-wide in most early pachytene spermatocytes (92%). At the onset of pachynema, sex chromosomes mostly displayed comparable H3.3 and H3.1/3.2 levels (Fig. 5A, B). However, this balance changed during the subsequent sub-stages of pachynema. Although robust H3.3 levels remained, H3.1/3.2 appeared excluded from the sex chromosomes in most mid (56%) and all late pachytene spermatocytes (Fig. 5A, B). In contrast, the loss of ARID1A increased the proportion of mid (66%) and late (40%) pachytene spermatocytes retaining H3.1/3.2 on sex-linked chromatin (Fig. 5B). The abnormal retention of canonical H3.1/3.2 coincides with a lack of H3.3 enrichment on sex-linked chromatin in response to the loss of ARID1A.

To determine whether these abnormal kinetics result from a genome-wide deficiency in H3.3, we compared its levels by Western blotting to find no difference in H3.3 abundance in *Arid1a*^{cKO} relative to *Arid1a*^{WT} spermatocyte enriched populations (Fig. S7A). We also considered an alternative possibility that ARID1A might promote the sex-linked enrichment of H3.3 by influencing the expression of cognate chaperones like DAXX and HIRA during murine pachynema (Rogers et al., 2004; van der Heijden et al., 2007). We addressed this by monitoring DAXX and HIRA levels in response to the loss of ARID1A using IF. In the case of DAXX, we examined meiotic spreads to find no changes in either the overall levels or sex chromosome localization of DAXX in response to the loss of ARID1A (Fig. S7B). The same was also true of HIRA, whose levels and nuclear localization in mutants appeared comparable to that seen in

escaper (from *Arid1a*^{cKO}) and normal (*Arid1a*^{WT}) spermatocytes (Fig. S7C). Therefore, ARID1A impacts H3.3 accumulation on the sex chromosomes without affecting its expression during pachynema. Overall, our data suggest that ARID1A influences MSCI by regulating the composition of sex-linked chromatin.

ARID1A prevents the promoter accumulation of H3.3

To define the changes in the sex-linked associations of H3.3 at a higher resolution, we performed CUT&RUN on pachytene spermatocytes isolated from *Arid1a*^{WT} and *Arid1a*^{cKO} testes. Despite the appearance of a robust H3.3 IF signal from the sex body during normal pachynema (Fig. 5A), the Macs2 peak caller (Zhang et al., 2008) identified very few sex-linked peaks (n = 224). These peaks were overwhelmingly associated with intergenic regions (Fig. S8A). Comparatively, a dramatically higher number of peaks (n=12183) primarily associated with genic (promoter, intron, and exon) regions occurred in *Arid1a*^{cKO} pachytene spermatocytes (Fig. S8A). More interestingly, there appeared to be a shift from few but overwhelmingly sex-linked H3.3 peaks (n=224; 98%) to autosomal H3.3 peaks (n=11512; 94.5 %) in response to the loss of ARID1A (Fig. S8A). Additionally, while the proportion of H3.3 sex-linked peaks in *Arid1a*^{cKO} pachytene spermatocytes was few (n=671; 5.5%), they outnumbered their *Arid1a*^{WT} counterparts by 3-fold. These data suggest that the loss of ARID1A strongly influences H3.3 genomic associations.

Due to the increased representation of promoter-associated peaks in response to the loss of ARID1A, we monitored H3.3 association with TSSs of genes differentially regulated by ARID1A. Consistent with the genomic annotation of H3.3 peaks, we could not detect H3.3 enrichment at TSSs associated with ARID1A-regulated sex-linked genes relative to IgG control. H3.3 signal spread gene-wide in *Arid1a*^{WT} pachytene spermatocytes (Fig. S8B, Fig. S9A-top panel). In contrast, we observed a striking accumulation of H3.3 at the TSSs of sex-linked genes misexpressed without ARID1A (Fig. S8B, Fig. S9A). There is a transition from the gene-wide spreading of H3.3 to promoter-proximal enrichment in response to the loss of ARID1A. Concomitantly, X and Y-linked intergenic regions undergo a significant decrease in H3.3 occupancy upon ARID1A loss (Fig. S8A). A similar loss of H3.3 occupancy occurred at a handful of autosomal intergenic peaks (Fig. S8A, Fig. S9B - top).

Unlike the sex-linked targets, TSSs of ARID1A-regulated autosomal genes displayed H3.3 enrichment relative to the IgG control (Fig. S8C, Fig. S9B - bottom). However, this TSS

occupancy appeared enhanced in *Arid1a*^{cKO} relative to *Arid1a*^{WT} pachytene spermatocytes (Fig. S8C, Fig. S9B). Therefore, TSSs of both sex-linked and autosomal gene targets display concordant changes in H3.3 occupancy. Overall, ARID1A occupancy at TSSs (Fig.S5) of differentially regulated genes prevents the accumulation of H3.3 at target promoters.

ARID1A restricts H3.3 occupancy to intergenic regions on the sex chromosomes

Our analysis of the genome-wide localization of H3.3 in response to the loss of ARID1A would argue that the abnormal increase in promoter-associated H3.3 results from its redistribution from high-affinity sites (peaks) that are predominantly sex-linked and intergenic during normal pachynema (Fig. S8A, Fig. S9). We focused our attention on these H3.3-occupied intergenic sex-linked sites. Although the Macs2 algorithm identified only 224 sex-linked intergenic peaks, we speculated that this approach filtered out regions enriched for H3.3 that fail to meet the peak calling threshold compounded by the pervasive spreading of H3.3 on the sex chromosomes (Fig. 5A, Fig. S8B, S9A). We adopted an alternative strategy that involved identifying potential H3.3 bound sites by monitoring their occupancy at ARID1A-governed accessible chromatin (Fig. 4A). We compared *Arid1a*^{WT} and *Arid1a*^{cKO} pachytene spermatocyte associated ATAC-seq peaks to identify mutually exclusive and overlapping peaks using BEDTools (Quinlan and Hall, 2010). The resulting peaks cluster into lost (n=9), common (n=7194), or gained (n=2246) based on their absence, persistence, or appearance, respectively, in *Arid1a*^{cKO} relative to *Arid1a*^{WT} pachytene spermatocytes (Fig. 6A). Next, we examined the ATAC-seq signal at these regions to find an increase in accessibility not only at gained peaks as expected but also at common peaks in *Arid1a*^{cKO} relative to *Arid1a*^{WT} pachytene spermatocytes.

Despite being labeled as lost, these regions did not display the expected loss in ATAC-seq signal in *Arid1a*^{cKO} relative to *Arid1a*^{WT} pachytene spermatocytes (Fig. 6A, left panel). The ATAC signal appears unchanged, highlighting the possibility that lost regions were labeled as such because they failed to satisfy Macs2 peak thresholds in *Arid1a*^{cKO} pachytene spermatocytes, especially given the comparatively higher magnitude of ATAC signal surrounding the common and gained peaks (Fig. 6A, left panel). We restricted our analysis to common and gained sites constituting 99 % of sex-linked regions subject to ARID1A-regulated chromatin accessibility. By plotting the average H3.3 coverage at sites associated with common and gained peaks, we detected striking differences in H3.3 occupancy. Briefly, both common and gained open chromatin regions consisted of loci differentiated by either a loss or robust increase in H3.3 occupancy in *Arid1a*^{cKO} relative to *Arid1a*^{WT} pachytene spermatocytes (Fig. 6A, right panel). To

gain further insight, we performed k-means clustering, based on H3.3 occupancy, to identify 4 clusters associated with either common (C1-C4) or gained (G1-G4) peaks (Fig. 6B). The clusters associated with common ATAC-seq peaks displayed contrasting changes in H3.3 occupancy in response to the loss of ARID1A. C1 and C2 represented regions deficient for H3.3, while C3 and C4 represent regions that gained H3.3 binding in *Arid1a*^{cKO} relative to *Arid1a*^{WT} pachytene spermatocytes (Fig. 6B, right panel). Similarly, clusters associated with gained ATAC-seq peaks, namely, G1 and G3, represented sites that gained H3.3 occupancy, while G2 identified sites that lost H3.3 occupancy. In contrast to clusters G1-G3, regions associated with G4 displayed an unremarkable association with H3.3 in response to the loss of ARID1A (Fig. 6B, right panel). Genomic annotations of common and gained k-means clusters revealed that the sites that displayed a loss of H3.3 binding (represented by C1 + C2, G2) in response to the loss of ARID1A were intergenic (Fig. S10A).

In contrast, those that gained significant H3.3 localization (represented by C3, C4, and G1+G3) distributed differentially between intergenic and genic regions (Fig. S10A). Therefore, these data support our idea that ARID1A restricts H3.3 occupancy primarily to intergenic sites on the sex chromosomes. Furthermore, the loss of ARID1A triggers an abnormal redistribution of H3.3 to genic regions. Therefore, the increased promoter occupancy of H3.3 is an indirect consequence of ARID1A loss.

ARID1A-governed H3.3 localization influences the sex-linked association of DMC1

To gain further insight into the mechanisms regulating H3.3 associations on the sex chromosomes, we examined the regions associated with various k-means clusters to investigate the enrichment of relevant motifs. To our surprise, we detected an enrichment of the motif associated with the DSB hotspot specifier, PRDM9 (PR domain-containing protein 9), in clusters related to gained peaks, G1 and G3 (Fig. S10B, top). Additionally, we observed an increased frequency of PRDM9 motif centered at gained ATAC-seq peaks associated with G1 and G3 (Fig. S10B, middle).

Interestingly, regions associated with G1 and G3 are usually devoid of H3.3 (Fig. 6B), implying a potential antagonism between H3.3 occupancy and the occurrence of meiotic DNA DSBs. Gained ATAC-seq peaks associated with G2, which usually displays H3.3 occupancy, appeared devoid of PRDM9 motif occurrences relative to G1 and G3 (Fig. S10B, middle). Next, we determined the frequency of the PRDM9 motif at k-means clusters associated with common

ATAC-seq peaks. These regions also displayed a dichotomous association with H3.3 (Fig. 6B). C3 and C4, usually deficient in H3.3, showed an increased frequency of PRDM9 motifs relative to C2, which typically displays H3.3 binding (Fig. S10B, bottom). These data illustrate an antagonistic relationship between H3.3 and meiotic DNA DSBs.

Since the PRDM9 motifs identified from SSDS (Single-Stranded DNA Seq) data were generated to map the genomic associations of DNA repair factor DMC1(Brick et al., 2012), we monitored its enrichment at the various k-means clusters. We also monitored the association of markers of meiotic DNA DSBs, such as the PRDM9 catalyzed H3K4me3 at common and gained k-means clusters using published ChIP-seq data from pachytene spermatocytes (Maezawa et al., 2018a). Consistent with the motif analyses, DMC1 occupancy and H3K4me3 enrichment occurred at gained and common ATAC-seq peaks associated with k-means clusters, normally devoid of H3.3, namely, G1, G3, G4, C3, and C4 (Fig. S10 C, D).

These data suggest that ARID1A might indirectly influence DNA DSB repair on the sex chromosomes by regulating the localization of H3.3. To test this conclusion, we monitored the association of DMC1 on the sex chromosomes in response to the loss of ARID1A by IF. Normally, DMC1 foci appear distributed along the non-homologous arms of the X and Y chromosomes from early to mid-pachynema, only disappearing by late pachynema (Fig. 7A, left, panel insets) (Moens et al., 2002). In contrast, in the absence of ARID1A, we observed a marked reduction in the number of DMC1 foci (Fig. 7A, right, panel insets). Quantification of DMC1 foci in Arid1a^{cKO} relative to Arid1a^{WT} pachytene spermatocytes revealed a significant decrease in the sex-linked association of DMC1 in the absence of ARID1A (Fig. 7B). Along with DMC1, the mitotic DNA recombinase, RAD51, is also known to localize to the non-homologous arms of the sex chromosomes (Moens et al., 1997; Moens et al., 2002). Therefore, we determined whether ARID1A also influenced the sex-linked association of RAD51. First, we analyzed previously generated RAD51-SSDS data (Hinch et al., 2020) to monitor its enrichment across the various k-means clusters associated with common and gained ATAC-seq peaks. Unlike DMC1, we found no detectable levels of RAD51 at any k-means clusters (Fig. S11A). Furthermore, the formation of RAD51 foci along the asynapsed axes of the sex chromosomes appeared unchanged in *Arid1a*^{cKO} relative to *Arid1a*^{WT} pachytene spermatocytes (Fig. S11B). Therefore, ARID1A is necessary for the normal sex-linked association of DMC1 but not RAD51. More importantly, our data highlight a dual role for ARID1A in regulating sex chromosome repression and DNA repair (Fig. 8).

Discussion

We previously demonstrated a spermatogenic requirement for the mammalian SWI/SNF complex based on its role in coordinating germline transcription (Menon et al., 2019). Furthermore, we showed that the SWI/SNF PBAF subcomplex activates genes essential for reductional meiosis and gamete formation (Menon et al., 2021). These data highlight that distinct SWI/SNF subcomplexes govern specific meiotic transitions.

Our current study demonstrates a requirement for the ARID1A-associated BAF (BAF-A) subcomplex for meiotic sex chromosome inactivation (MSCI). It does so by promoting the accumulation of the variant histone H3.3 on the sex chromosomes at the onset of mid-pachynema, coinciding with the eviction of canonical histones H3.1/3.2 and RNA polymerase II from the sex body (Model, Fig. 8). In contrast, when depleted of ARID1A, chromatin accessibility increased along with a deficiency of H3.3 and the continued presence of H3.1/3.2 and pSer2-RNAPII (an elongating form of RNA polymerase II) in the sex body. These data indicate that BAF-A helps define features distinguishing sex chromosomes from autosomes and that the absence of the BAF-A subcomplex during meiosis I results in the failure of MSCI during pachynema.

Although previous work described the association of H3.3 with the sex body (van der Heijden et al., 2007; Yuen et al., 2014) and its requirement for meiotic repression of sex-linked genes (Fontaine et al., 2022), our study revealed the need for BAF-A in the preferential localization of H3.3 to the sex body relative to autosomes. Interestingly, a similar role for BAF-A in promoting H3.3 incorporation occurs in human endometriotic cells (Reske et al., 2022). In this case, the genomic localization of H3.3 to super-enhancers required ARID1A. Our study describes the ARID1A-dependent localization of H3.3 at a chromosome-wide scale comprised of (i) local enrichment at intergenic loci and (ii) larger domains that resembled spreading much like that of *Xist* during female X chromosome inactivation (XCI) (Chaumeil et al., 2006). X chromosome inactivation (XCI) requires SWI/SNF subunits SMARCA4 and SMARCC1 in female mouse embryonic stem cells (mESC) (Keniry et al., 2022). SMARCC1 promotes XCI by increasing promoter accessibility of the inactive X chromosome (Xi). Interestingly, during MSCI, sex-linked chromatin displays enhanced accessibility (Maezawa et al., 2018b). In contrast, our studies showed that BAF-A limits rather than enhances sex-linked chromatin accessibility. These data highlight a mechanism that checks chromosome-wide relaxation during MSCI. The divergent

outcomes of SWI/SNF-governed sex-linked chromatin accessibility during XCI and MSCI probably reflect noticeable sex-specific differences or arise from potentially perturbing distinct SWI/SNF subcomplexes.

Along with altered chromatin composition and structure, pachytene spermatocytes lacking ARID1A also displayed an abnormal association of pSer2-RNAPII (elongating form) with the sex body. Normally, total transcriptional output peaks towards the end of meiotic prophase-I, even with MSCI coinciding (Alexander et al., 2022; Ernst et al., 2019; Monesi, 1964). The dynamic switching from the paused (pSer5-RNAPII) to the elongating (pSer2-RNAPII) state of RNAPII drives this burst of transcription on autosomes (Alexander et al., 2022). The association of pSer2-RNAPII with the sex chromosomes without ARID1A renders them more autosome-like, underlying the defect in sex-linked gene repression. The BAF-A-governed H3.3 dynamics on the sex chromosomes may limit the switch from the paused to the elongating state of RNAPII. In a human cell culture model, ZMYND11, a known tumor suppressor and reader of Lysine 36 trimethylation on H3.3 (H3.3K36me3), suppresses RNAPII elongation (Wen et al., 2014). Whether similar H3.3 readers affect RNAPII pausing during meiosis in mice remains unknown.

The initiation and maintenance of MSCI are known to be regulated by DNA damage response (DDR) factors, ATR, and MDC1, respectively (Ichijima et al., 2011; Royo et al., 2013; Turner et al., 2004). However, ARID1A deficient pachytene spermatocytes appeared proficient in sex-linked DDR signaling, evidenced by the normal enrichment of ATR, γH2Ax, and MDC1 on the sex body. Therefore, BAF-A-mediated transcriptional repression of the sex chromosomes occurs independently of DDR signaling. Given that the accumulation of ATR and MDC1 on the sex body precedes that of ARID1A, which only manifests late in diplonema, it is reasonable to hypothesize that DDR signaling might recruit BAF-A to the sex chromosomes.

ARID1A did not appear necessary for sex-linked DNA DSB formation. In contrast, the expected association of DMC1, the meiosis-specific DNA recombinase, with the asynapsed axes of the sex chromosomes do require ARID1A. Interestingly, sex-linked intergenic sites displaying an ARID1A-dependent enrichment of H3.3 appeared depleted for DMC1. Consistent with this antagonism, the loss of ARID1A resulted in the re-distribution of H3.3 to regions normally associated with DMC1. However, a subset of normal DMC1-associated regions (G4) displaying a distinct chromatin composition with little or no occupancy of H3.3 may undergo different dynamics of ARID1A regulation. Although only correlative, these data suggest that regions

displaying a localized enrichment of H3.3 might be unfavorable for DNA repair. Determining the extent to which a deficiency in BAF-A activity might impede sex-linked DNA repair is challenging. RAD51 binding to the sex chromosomes remained stable without ARID1A, suggesting that some sex-linked DNA repair remains. Furthermore, RAD51 and DMC1 bind ssDNA at PRDM9/SPO11 designated DSB hotspots. However, these recombinases occupy unique domains. DMC1 localizes nearest the DSB breakpoint, promoting strand exchange, whereas RAD51 is further away (Hinch et al., 2020). Here, we show that loss of ARID1A decreases DMC1 foci on the XY chromosomes without affecting RAD51. These findings indicate that BAF-A plays a role in the loading and/or retention of DMC1 to the XY chromosomes. Our studies highlight a model in which BAF-A promotes meiotic progression by facilitating MSCI and DNA repair on the sex chromosomes.

Materials and Methods

Generation of *Arid1a* conditional mutant mice

Generation of the *Arid1a*^{tm1Mag}/Mmnc mutant allele was previously described (Chandler et al., 2015). The mice are available through the regional mutant mouse resource and research center (MMRRC; Stock number: 041418-UNC; www.mmrrc.org). *Arid1a* floxed mice (*Arid1a*$^{tm1Mag/}$*Mmnc*) exist on a CD1 genetic background. Crosses with testes-specific *Stra8-Cre* mice (expressed in P3 spermatogonia) (Sadate-Ngatchou et al., 2008) resulted in conditional knockouts. *Arid1a*$^{fl/fl}$; *Stra8- Cre*$^{Tg/0}$ females were crossed to either *Arid1a*$^{fl+}$ or *Arid1a*^{flfl} males to obtain *Arid1a*^{flfl};*Stra8-Cre*$^{Tg/0}$ (*Arid1a*^{cKO}) and either *Arid1a*^{flfl} or *Arid1a*$^{fl+}$ (*Arid1a*^{WT}) males. Haploinsufficiency associated with *Arid1a* negated the possibility of transmitting the Cre through the paternal germline. Genotyping primers: *Arid1a*$^{fl+}$ alleles - (F)- 5' - CTAGGTGGAAGGTAGCTGACTGA -3'; (R) 5' - TACACGGAGTCAGGCTGAGC -3' (PCR product sizes- *fl*: 300 bp; +: 200 bp), and *Stra8-Cre* - (F) 5' -GTGCAAGCTGAACAACAGGA-3', (R) 5' -AGGGACACAGCATTGGAGTC-3' (PCR product size- *Cre*: 150 bp). Mice were housed with a 12-hour light cycle (temperature - 20-24° C, humidity - 30-70%). All animal work followed approved UNC Chapel Hill IACUC protocols.

Histology

Arid1a^{WT} and *Arid1a*^{cKO} testes and cauda epididymites were fixed overnight in Bouins solution (Fisher Scientific Ricca chemical; 11-201) at 4° C, followed by dehydration in ethanol series (50%, 70%, and 100%) before embedding in paraffin. The animal histopathology core prepared

stained tissue sections (hematoxylin and eosin for cauda epididymites; Periodic acid-Schiff for testes). Staining and morphology determined seminiferous tubule staging (Ahmed and de Rooij, 2009; Meistrich and Hess, 2013). A summary of staging is provided (Supplementary Table 2).

Immunofluorescence staining of testis cryosection and spermatocyte spreads

Testes cryosections and spermatocyte spreads from juvenile (P18, P19, and P26) and adult *Arid1a*^{WT} and *Arid1a*^{cKO} mice were examined with indirect immunofluorescence (IF). 8-10 µm thick cryosections of testes were prepared using published methods (Menon et al., 2021). Whole testes were fixed in 10% neutral buffered formalin (NBF) at 4° C for 20 minutes. They were cut in half, followed by 40 minutes of incubation in 10% NBF. Fixed tissues were washed three times (10 minutes per wash) in room temperature (RT) phosphate-buffered saline (PBS) pH7.4. The tissues were then treated with a series of sucrose washes - 10% (30 min), 20% (30 min), and 30% (1 hr). Tissues were then incubated at 4° C overnight in a 1:1 ratio of a solution of 30% sucrose/optimum cutting temperature (OCT, Tissue-Tek; 62550-01), followed by embedding in OCT, sectioning, and storage at -80^{0} C. Before immunostaining, cryosections were thawed on a heating block at 42^{0} C, rehydrated for 10 minutes in PBS, and incubated in 10mM citric acid buffer (pH6.0) for 10 minutes at 80-90^{0} C (antigen retrieval), during which addition of fresh citrate buffer (80-90 ^{0}C) occurred every 2 minutes, and then allowed to cool for 20 minutes. For immunostaining, cryosections were incubated overnight in a humidified chamber with primary antibodies (Supplementary Table 3) at 4^{0} C and then followed by a secondary antibody incubation at RT for 1 hr. Sera were diluted with antibody dilution buffer in PBS (ADB: 3% bovine serum albumin; 10% goat serum; 0.5% Triton-X 100). Two identical blocking steps preceded antibody incubations. These steps involved sequential incubations in (i) PBS, (ii) PBS/0.1% Triton-X 100, and (iii) blocking solution (1:10 dilution of ADB in PBS) for 10 minutes each at RT. Immunostained slides were washed twice in Kodak Photo-Flo 200 (PBS/0.32%), counterstained with DAPI, washed again in PBS/0.32% Photo-Flo 200, and then mounted in Prolong Gold antifade medium (P-36931; Life Technologies).

Spermatocyte spreads were prepared as previously described (Gray et al., 2020) with minor modifications. Briefly, seminiferous tubules were incubated in hypotonic buffer (30mM Tris pH8.2, 50mM Sucrose, 17 mM Trisodium dihydrate, 5mM EDTA, 0.5mM DTT, 0.1 mM PMSF) for 10-20 minutes on ice. Tubules were minced in 100 mM sucrose (200 µL/testis) until the solution turned turbid. The resulting cell suspension was isolated, avoiding tissue debris, and held on ice. Cells were fixed and spread by dropping 20 µL of cell suspension directly onto glass

slides coated with paraformaldehyde solution (1 % Paraformaldehyde; 0.15 % Triton X-100; 625 nM Sodium Borate, pH 9.2). Uniform spreading was ensured by tilting the slides along the near and opposite edges. Next, slides were incubated in a humidified chamber for 1 hr, following which they quickly air-dried and then washed two times in PBS/0.32% Photo-Flo 200 and once in H_2O/0.32% Photo-Flo 200. Air-dried slides were immediately processed for immunostaining as described above for cryosections or stored at - 80^0 C. Immunostained spreads were washed 2x with PBS/0.32% Photo-Flo 200, counterstained with DAPI, and washed again with Photo-Flo 200. Stained spreads were mounted in Prolong Gold antifade medium. The list of antibodies for IF is provided in supplementary table 3. The Leica Dmi8 fluorescent microscope was used to capture images. Z-stacks were deconvoluted using Leica Dmi8 image software (Huygens essentials version 20.04). Some whole immunofluorescence image panels with low visibility (see figure legends 3,5 and supplemental figure legends 4,6,7) were enhanced to increase brightness.

Fluorescence intensity measurements and object (foci) counting were performed with Fiji (Schindelin et al., 2012). RNAPII (pSer2) IF signal intensities were measured using the method described previously (Menon et al., 2021). Briefly, pixel intensities were recorded from regions of interest (ROI), which include the sex chromosomes (sex body) and an area lacking cells (background fluorescence). Corrected total RNAPII-pSer2 fluorescence (CTRF) was calculated using the method previously described (https://theolb.readthedocs.io/en/latest/imaging/measuring-cell-fluorescence-using-imagej.html), where CTRF= Integrated density associated with sex body – (Area of sex body x Mean fluorescence of background).

For counting axial DMC1 foci, images were cropped to an area encompassing the sex chromosomes. Cropped images were converted to 8-bit grayscale, and the DMC1 fluorescent channel selected for further processing. An ROI was set, manual thresholding was performed to select DMC foci, and noise (speckles) removed using the Fiji median filter tool with a radius set to 2.0-4.0. Finally, DMC1 was enumerated with the count particles tool. Statistical significance was calculated using an unpaired student's t-test. Metadata associated with the quantification of RNAPII (pSer2) fluorescence and DMC1 foci are provided (Supplementary Table 4,5)

Preparation of acid-extracted histones and western blotting

Histones from P19 *Arid1a*^{WT} and *Arid1a*^{cKO} spermatogenic cells were acid-extracted using published methods (Shechter et al., 2007). Seminiferous tubules were digested in 1 mL of Enriched Krebs-Ringer Bicarbonate (EKRB) Medium (EKRB salts - 1.2 mM KH_2PO_4, 1.3 mM $CaCl_2$, 119.4 mM NaCl, 4.8 mM KCl, 1.2 mM $MgSO_4$, 11.1 mM Dextrose; 25.2 mM $NaHCO_3$; 1X essential amino acids -Invitrogen, 11130051; 1X non-essential amino acids-Gibco,11140050) supplemented with 0.5 mg/mL collagenase (10 minutes, rotated at 32 ^{o}C). Digested tubules sedimented by gravity for 5 minutes at RT. The supernatant was removed, tubules were resuspended in 1 mL EKRB medium, and then settled for 5 minutes at RT. The sedimented tubules were transferred to 1 mL EKRB medium supplemented with 0.025% trypsin and 4 µg/mL DNase-I. The suspension was incubated for 10 minutes on a rotator at 32° C. Digestion was halted with 10% Fetal bovine serum (FBS), and single-cell suspensions were prepared by pipetting the slurry and then filtering it sequentially through 70 µm and 40 µm filters. Cells were pelleted at 600g for 5 minutes, washed once in PBS, and processed for histone extraction. Briefly, cell pellets were resuspended in 1 mL hypotonic lysis buffer (10mM Tris-Cl pH8.0, 1mM KCl, 1.5mM $MgCl_2$, 1mM DTT) and incubated on a rotator at 4° C for 30 minutes. Nuclei were pelleted at 10,000 g for 10 minutes at 4° C. Nuclear pellets were resuspended in 400 µL 0.2N HCl and incubated for 1 hr at 4 ^{o}C, followed by centrifugation at 14,000 g for 10 minutes at 4° C to isolate supernatants containing histones that were precipitated with Trichloroacetic acid (TCA), and then added to the nuclear suspension at a final concentration of 33% and incubated on ice for 30 minutes. Precipitated histones were pelleted at 14,000g for 10 minutes at 4° C and washed two times in 1 mL ice-cold acetone. Finally, washed histones were air-dried at RT for 20 minutes and resuspended in 100 µL ddH_2O. Histones were separated on a 15 % SDS-polyacrylamide gel for western blots and transferred to a PVDF (Polyvinylidene Difluoride) membrane using a semi-dry transfer apparatus (Bio-Rad). Sample loading was assessed by REVERT^{TM} total protein stain (LI-COR, 926-11010). Blots were scanned on a LI-COR Odyssey CLx imager and viewed using Image Studio Version 5.2.5. Antibodies and their corresponding dilutions are listed (Supplementary Table 3).

Isolation of Pachytene Spermatocytes by the Sta-Put Method of Unit Gravity and Western Blotting

Pachytene spermatocytes were purified from *Arid1a*^{WT} and *Arid1a*^{cKO} adult testis by the unit gravity sedimentation procedure using a Sta-Put apparatus (Bellvé, 1993; O'Brien, 1993). Testis from at least 12 adult males (>P60) were dissected into EKRB, decapsulated, and digested in 0.5mg/ml collagenase for 15 min at 32° C. The resulting tubules were gently washed with EKRB

and digested with 0.25mg/ml trypsin supplemented with 4µg/ml DNase for 15 min at 32° C. Following trypsin incubation, additional DNase (4µg/mL) was added to reduce viscosity further. Samples were triturated for 3 minutes with a plastic transfer pipet to fragment flagella, break intercellular bridges between germ cells, and further disperse cells into suspension. Trypsin digestion was stopped by adding 0.25mg/mL trypsin inhibitor (Sigma/EPRO, T9003), and cell aggregates were removed by filtration using 40 µm cell strainers. Cells from the flow-through were pelleted at 500g for 5 min at 4° C, resuspended in EKRB + 0.5% BSA, and adjusted to a 3.33x10^{8} cells/mL density. 10^{9} cells from this single-cell suspension were loaded onto a 2-4% linear BSA gradient and allowed to sediment in the Sta-Put apparatus at 4° C. After 2hr and 40min of undisturbed sedimentation, 10ml fractions were collected at 45 sec per tube. Fractions were pelleted at 500g for 5 min at 4°C and resuspended in 1ml EKRB + 0.5%BSA. Fractions containing >80% pachytene spermatocytes were identified by light microscopy, pooled, and stored in cryoprotective media (DMEM supplemented with 10%FBS and 20%DMSO) at -80° C pending further analysis.

Pachytene spermatocytes obtained were resuspended in RIPA buffer (50mM Tris-HCl pH 8.0, 150mM NaCl, 1% NP-40, 0.5% Sodium deoxycholate, 0.1% SDS, 5mM NaF, 1mM Na_3VO_4, 1mM Phenylmethylsulfonyl fluoride (PMSF), 1X Protease inhibitor cocktail (Sigma)) at 4˚C and sonicated for 15 minutes followed by centrifugation at 12000xg for 10 minutes at 4˚C. Western blotting was performed by separating samples in 5% SDS-polyacrylamide gel and transferring to PVDF (polyvinylidene difluoride) membranes (Bio-Rad) overnight. Blots were scanned on a LI-COR Odyssey CLx imager and viewed using Image Studio Version 5.2.5. Antibodies and their corresponding dilutions are listed (Supplementary Table 3).

RNA extraction and RT-PCR

Total RNA was isolated in TRIzol™ reagent (Invitrogen, 15596026) from Sta-Put purified fractions enriched for pachytene spermatocytes and round spermatids. The extracted RNA was purified using the Direct-zol RNA kit (Zymo, R2050). cDNA was synthesized using a random primer mix (New England Biolabs, S1330S) and ProtoScript® II reverse transcriptase (New England Biolabs, M0368L). RT-PCR was performed on 1:10 cDNA dilutions using Sso Fast EvaGreen supermix (Bio-Rad, 172-5280) on a thermocycler (BioRad, C1000). Amplicons associated with either floxed or excised *Arid1a* cDNA's were detected using primers: (F)- 5$^{'}$-TCCAGTAAGGGAGGGCAAGAAGAT -3$^{'}$; (R) 5$^{'}$- GTAGTTGGCGTTGGGCAAGGCATTA -3$^{'}$ (PCR product sizes- *fl*: 612 bp; *Δ*: 281 bp)

RNA-seq

RNA was extracted and purified in quadruplicate from frozen pellets of *Arid1a*^{WT} and *Arid1a*^{cKO} pachytene spermatocytes obtained by Salmony Sta-Put gravity sedimentation using the abovementioned methods. All samples displayed RNA integrity number (RIN) > 7.0 as determined by Agilent Tapestation (High sensitivity RNA screen tape). Sequencing libraries were prepared from 1 µg of total RNA using a Kapa mRNA HyperPrep kit (Roche, KK8580) per the manufacturer's instruction. Libraries were quantified using Qubit™ dsDNA Hs assay kit (Invitrogen, Q32854) pooled at equimolar concentrations, and sequenced on a single lane of the Illumina NovaSeq 6000 S Prime flow cell (50 bp reads, paired-end).

RNA-seq data analysis

Gene expression was quantified using Salmon (Patro et al., 2017). Transcript counts at the gene level were summarized using tximport (Soneson et al., 2016) and then imported to perform a differential gene expression analysis using DESeq2 (Love et al., 2014). The mouse (mm10) gene/transcript annotations were retrieved using AnotationDbi (Pàges et al., 2021) and *TxDb.Mus musculus.UCSC.mm10.known gene (Bioconductor Core Team, 2019)* R packages from Bioconductor. Low-count genes (< 10 reads) were pre-filtered, and significant differences in counts were called at a false discovery rate (FDR)≤ 0.05. Supplementary Table 6 lists differentially expressed genes.

CUT&RUN (Cleavage Under Targets and Release Using Nuclease)

CUT&RUN assays were performed on cryopreserved *Arid1a*^{WT} and *Arid1a*^{cKO} pachytene spermatocytes (500,000 cells/genotype) obtained by Sta-Put, using a slightly modified version of previously described methods (Meers et al., 2019; Skene and Henikoff, 2017). For ARID1A, CUT&RUN was performed in triplicates per genotype with two different antibodies. H3.3 CUT&RUN was performed in duplicates on *Arid1a*^{WT} and triplicates on *Arid1a*^{cKO} samples. Aliquots of cryopreserved *Arid1a*^{WT} and *Arid1a*^{cKO} pachytene spermatocytes were quickly thawed in a water bath at room temperature (RT), pelleted at 600g for 5 minutes, and washed [wash buffer: 20mM HEPES(Na) pH7.5, 150 mM NaCl, 0.5 mM spermidine, EDTA-free protease inhibitor] three times. Cells were gently resuspended in wash buffer and bound to Concanavalin-A coated magnetic beads (20 µL beads/500,000 cells) by mixing on a rotator for 15 minutes. The bead slurry was separated using a magnet followed by permeabilization in 50 µL antibody buffer (wash buffer + 0.05% Digitonin + 2mM EDTA) per sample in 0.2 mL 8-strip PCR tubes.

714 Primary antibody was added to the samples and incubated on a nutator at 4° C overnight. Cells
715 were then separated using a magnet, washed two times in 200 µL Dig-wash buffer (wash buffer
716 + 0.05% Digitonin), and incubated with a secondary antibody prepared in 50 µL of Dig-wash
717 buffer/sample for 30 minutes on a nutator at 4° C. After antibody incubations, samples were
718 washed twice in 200 µL Dig-wash buffer and then incubated on a nutator at 4° C with 50 µL Dig-
719 wash buffer containing 1000ng/mL Protein A/G Micrococcal Nuclease (pA/G-MNase) for 1 hr.
720 Following this, samples were washed twice in 200 µL Dig-wash buffer, resuspended in 50 µL
721 Dig-wash buffer, cooled down to 0° C, and supplemented with $CaCl_2$ at a final concentration of 2
722 mM to activate MNase. Samples were digested at 0 ^{o}C for 40 minutes. The resulting chromatin
723 fragments were extracted from the bead slurry by incubating in 2X STOP buffer (340 mM NaCl,
724 20mM EDTA, 4mM EGTA, 0.05% Digitonin, 100 µg/mL RNase A) at 37° C for 30 minutes. DNA
725 was purified using ChIP DNA clean and concentrator kit (Zymo, D5205). Libraries were
726 prepared using the Kapa Hyperprep kit (Roche, KK8504), examined for size, and quantified on
727 an Agilent 2100 bioanalyzer using the high-sensitivity DNA kit (Agilent, 5067-4626). The
728 libraries were pooled in equimolar amounts and sequenced on a single lane of the Illumina
729 NovaSeq 6000 S Prime flow cell (50 bp reads, paired-end). Antibody details are listed in
730 Supplementary Table 3. The pA/G-MNase (Addgene ID: 123461) used for the CUT&RUN
731 experiments was purified at UNC-Chapel Hill's Protein Expression and Purification core.
732
733 **CUT&RUN data analysis**
734 CUT&RUN data analyses were performed as previously described (Menon et al., 2021). Briefly,
735 fastq files were analyzed with fastqc (version 0.11.9), then processed with TrimGalore (version
736 0.6.2, https://www.bioinformatics.babraham.ac.uk/projects/trim_galore/) keeping the --trim-n
737 option. Trimmed reads were aligned to mm10 (mouse) reference genome using bowtie2
738 (Langmead and Salzberg, 2012) parameters: bowtie2 --very-sensitive-local --no-mixed --no-unal
739 --dovetail --no-discordant. Alignments were outputted in BAM format using samtools (Li et al.,
740 2009) and filtered for PCR duplicates using Picard tools, MarkDuplicates
741 (https://broadinstitute.github.io/picard/). Deduplicated BAM files were used to generate bigWig
742 files filtered for ENCODE mm10 blocked regions (Amemiya et al., 2019) with DeepTools,
743 bamCoverage (Ramírez et al., 2016) with the following options: -bs 30 --smoothLength 60 -bl --
744 scaleFactor. The option --scaleFactor was used to normalize for composition bias between
745 CUT&RUN libraries generated from *Arid1a*^{WT} and *Arid1a*^{cKO} pachytene spermatocytes.
746 csaw (Lun and Smyth, 2015) derived normalization factors (nf) were used to calculate the
747 effective library size (library size X nf). The inverse of the effective library size per million was

supplied to --scaleFactor to generate normalized bigWig files. Peak calling was performed with MACS2 (version 2.1.2) with options: -f BAMPE --broad --broad-cutoff 0.05 --keep-dup all, on filtered BAM files associated with ARID1A and H3.3 relative to an IgG control previously generated from pachytene enriched populations obtained from P18 testes (Chakraborty and Magnuson, 2022). Peak overlaps across replicates were determined using bedtools intersect (Quinlan and Hall, 2010). Peak calls are provided in supplementary table 7. Peaks were annotated using HOMER (version 4.9.1), annotatePeaks.pl. Replicate bigWig files were averaged using WiggleTools (Zerbino et al., 2014). Averaged bigWig files generated heatmaps with DeepTools, computeMatrix, and plotHeatmap. Data was visualized on Integrative Genomics Viewer (Robinson et al., 2011).

ATAC-seq

Cryopreserved aliquots of *Arid1a*^{WT} and *Arid1a*^{cKO} pachytene spermatocytes were processed in quadruplicate for ATAC-seq using the standard Omni-ATAC protocol (Corces et al., 2017) with minor changes. These involved increasing the cell number to 100,000 per replicate, using Diagenode tagmentase (loaded Tn5 transposase, C01070012) and Diagenode 2X tagmentation buffer (C01019043). Libraries were quantified using NEBNext® kit for Illumina® (New England Biolabs, E7630S), pooled at equimolar amounts, and sequenced on a single lane of the Illumina NovaSeq 6000 S Prime flow cell (50 bp reads, paired end).

ATAC-seq data analysis

After analyzing the quality of fastq files with fastqc (version 0.11.9), they were processed with TrimGalore (version 0.6.2), keeping the --trim-n option. Alignments to mm10 reference genome were performed with bowtie2 (Langmead and Salzberg, 2012) parameters: bowtie2 --very-sensitive -X 2000, and outputted in BAM format using samtools. Resultant BAM files were filtered for PCR duplicates using Picard tools, MarkDuplicates, and mitochondrial reads using samtools view (code: samtools view -h Dedup.bam | grep -v 'chrM' | samtools view -b -h -f 0x2 - | samtools sort > Dedup_noChrM.bam). Filtered BAM files were used to call peaks with MACS2 (parameters: -f BAMPE -n de -q 0.05 --nomodel --nolambda --keep-dup all) and generate normalized bigWig files with DeepTools, bamCoverage (options: -bs 30 --smoothLength 60 -bl --normalized using RPKM). Peak overlaps across replicates were determined using bedtools intersect (Quinlan and Hall, 2010). Peak calls are provided in supplementary table 8. Peak annotation (annotatePeaks.pl) and motif analyses (findMotifsGenome.pl) were performed with HOMER (version 4.9.1). PRDM9 motif frequency near ATAC-seq peaks was determined using

HOMER annotatePeaks.pl with options: -size 20000 -hist 10. Replicate bigWig files were averaged using WiggleTools (Zerbino et al., 2014). Averaged bigWig files generated heatmaps with DeepTools, computeMatrix, and plotHeatmap. Data was visualized on Integrative Genomics Viewer (Robinson et al., 2011).

DATA AVAILABILITY:

RNA-seq, CUT&RUN, and ATAC-seq data generated in this study are deposited with GEO (Gene Expression Omnibus) under accession number GSE225612. DMC1 SSDS (GSE35498), RAD51 SSDS (GSE143582), and H3K4me3 ChIP-seq (GSE89502) datasets were previously published (Brick et al., 2012; Hinch et al., 2020; Maezawa et al., 2018a) and are available on GEO.

ACKNOWLEDGEMENTS

We thank Magnuson lab members for their helpful comments on manuscript preparation. Next-generation sequencing was performed at the Duke Center for Genomic and Computational Biology. pA/G-MNase was produced by the Protein Expression and Purification core at the University of North Carolina at Chapel Hill (supported by Cancer Center Support Grant, P30 CA16086). We thank Dr. Atilla Töth (Technishe Universität Dresden) for generously providing the HORMAD1 antibody. This work was supported by National Institutes of Health grants R01GM101974 (T.M).

AUTHOR CONTRIBUTIONS

D.U.M and T.M conceptualized and designed the project. D.U.M., PC, and N.M. carried out experiments. Data curation and validation are done by D.U.M, PC, and N.M. D.U.M, PC, and NM performed the writing, which was reviewed and edited by T.M. Project supervision and funding acquisition by T.M.

COMPETING INTERESTS

The authors declare no competing interests.

Figure Legends

Fig 1. ARID1A associates with the sex body late in meiotic prophase-I.
Representative wild-type pachytene and diplotene spermatocyte spreads immunolabelled for ARID1A (magenta) and SYCP3 (green) and then counterstained for DNA (blue). Panel insets denote a magnified view of the nuclear area surrounding the sex chromosomes. Scale bar:10 µm, magnification: 100x.

Fig 2. Requirement of ARID1A for the repression of sex-linked genes.
(A) MA plot describing the LOG2-fold-change (LFC, y-axis) in mean expression (x-axis) of genes displaying significant (FDR≤0.05, magenta dots) changes in *Arid1a*^{cKO} relative to *Arid1a*^{WT} pachytene spermatocytes. Dashed blue lines denote 2 LFC. Gray dots (FDR≥0.05) depict non-significant changes in gene expression. (B) Violin plot describing the LOG2-fold-change (LFC, y-axis) in the median chromosome-wide gene expression (x-axis) in *Arid1a*^{cKO} relative to *Arid1a*^{WT} pachytene spermatocytes. The dashed blue line denotes no change in gene expression.

Fig 3. ARID1A limits RNA polymerase II (RNAPII) localization to the sex body.
(A) *Arid1a*^{WT} and *Arid1a*^{cKO} pachytene spermatocytes immunolabelled for pSer2-RNAPII (green), SYCP3 (cyan), and counterstained with DAPI (blue). Scale bar:15 µm, magnification: 100x. The sex chromosomes (white arrow) and sex body (yellow dashed circle) are labeled. Brightness of the whole image panel (A) was increased by compressing the dynamic range of the image panel using Adobe photoshop (0-1-255 to 0-1-150). (B) Dot plot describing the corrected total pSer2-RNAPII fluorescence (y-axis) measured from *Arid1a*^{WT} (n = 82) and *Arid1a*^{cKO} (n= 119) pachytene spermatocytes (3 replicates per genotype). Empty diamonds (magenta) represent independent data points. Significance determined by a two-tailed unpaired Student's t-test p values. Data expressed as mean (black dot) ± SEM.

Fig 4. ARID1A limits promoter accessibility.
(A) Genomic associations of MACS2 derived ATAC-seq peak calls from *Arid1a*^{WT} and *Arid1a*^{cKO} pachytene spermatocytes. Percent (%) distribution of genomic annotations is indicated. (B-C) Heatmap (bottom) and metaplot (top) displaying the average ATAC-seq signal associated with differentially expressed (B) autosomal and (C) sex-linked genes in *Arid1a*^{WT} and *Arid1a*^{cKO} pachytene spermatocytes. (B-C) The number of RefSeq annotations (n) associated with

differentially regulated genes (rows) is indicated. Up-reg: misexpressed, and Dn-reg: misrepressed genes in response to the loss of ARID1A. Average ATAC-seq coverage was plotted across RefSeq genes ± 3Kb.

Fig 5. ARID1A influences the chromatin composition of the sex body.

(A-B) *Arid1a*^{WT} and *Arid1a*^{cKO} pachytene spermatocytes immunolabelled for HORMAD1 (magenta), (A) ARID1A (cyan) and H3.3 (green), (B) ARID1A (green) and H3.1/3.2 (cyan). (A-B) Proportion (%) of *Arid1a*^{WT} and *Arid1a*^{cKO} early, mid, and late pachytene spermatocytes displaying distinct (A) H3.3, (B) H3.1/3.2 localization patterns with the sex body. For H3.3 immunostaining, the total number of *Arid1a*^{WT} pachytene spermatocytes: early = 144, mid= 274, late= 95; *Arid1a*^{cKO} pachytene spermatocytes: early = 43, mid= 86, late= 55, were scored, from 3 replicates each. For H3.1/3.2 immunostaining, the total number of *Arid1a*^{WT} pachytene spermatocytes: early = 91, mid= 124, late= 45; *Arid1a*^{cKO} pachytene spermatocytes: early = 22, mid= 116, late= 58, were scored, from 3 replicates each. DNA counterstained with DAPI (blue). The sex chromosomes (yellow arrow) and sex body (yellow dashed circle) are labeled. Scale bar:15 µm, magnification: 100x. Brightness of the whole image panel (Fig. 5) was increased by compressing the dynamic range of the image panels using Adobe photoshop (0-1-255 to 0-1-150).

Fig 6. H3.3 displays differential occupancy across ARID1A-governed sex-linked open chromatin.

(A-B) Heatmaps (bottom) and metaplots (top) displaying average (A) chromatin accessibility (purple heatmap) and H3.3 enrichment (green heatmap) associated with lost, common, and gained ATAC-seq peak calls (MACS2), (B) enrichment of H3.3 at k-means clusters associated with common (C1-C4, left) and gained (G1-G4, right) ATAC-seq peaks, in *Arid1a*^{WT} and *Arid1a*^{cKO} pachytene spermatocytes. (A-B) ATAC-seq and H3.3 coverage plotted over a 5 Kb window centered at ATAC-seq peaks (MACS2). Number of ATAC-seq peak calls (n) associated with each category is indicated.

Fig 7. ARID1A influences the axial association of DMC1 with the XY during pachynema.

(A) *Arid1a*^{WT} and *Arid1a*^{cKO} pachytene spermatocytes immunolabelled for HORMAD1 (magenta), ARID1A (green), DMC1 (cyan), and counterstained with DAPI (blue). Scale bar:15 µm, magnification: 100x. A magnified view of the sex chromosomes is indicated (yellow dashed square). (B) Dot plot displaying the number of sex-linked DMC1 foci (y-axis) quantified from

Arid1a^{WT} (n = 66) and *Arid1a*^{cKO} (ARID1A^{-}, n= 75) pachytene spermatocytes, obtained from 3 replicates each. Empty diamonds (magenta) represent independent data points. Significance determined using a two-tailed unpaired Student's t-test p values. Data expressed as mean (black dot) ± SEM.

Fig 8. A model describing the role of ARID1A sex-linked chromatin regulation.
During meiosis, the sex chromosomes undergo transcriptional repression at the onset of pachynema. A dramatic change in the composition of sex-linked chromatin accompanies this chromosome-wide repression. From mid to late pachynema, spermatocytes display a hyper-accumulation of the variant histone H3.3 (Ochre shading and gradient) on the sex chromosomes (magenta) relative to autosomes (green). Concomitantly, the canonical histones H3.1/3.2 levels and elongating pSer2-RNAPII complex (grey gradients) appear depleted from the sex body by late pachynema. The loss of ARID1A dramatically alters the chromatin composition of the sex body, which features low H3.3 (yellow bar) association at levels indistinguishable from autosomes throughout pachynema. Concomitantly, canonical H3.1/3.2 and pSer2-RNAPII levels (grey bar) on the sex body remain abnormally stable throughout pachynema. These sex-linked chromatin aberrations, along with persistent transcription owing to the association of pSer2-RNAPII with mutant sex body, fail meiotic sex chromosome inactivation (MSCI) and, consequently, pachytene arrest. This defect also coincides with an abnormal loss of DMC1 (blue foci) localization to the unpaired sex chromatids in response to the loss of ARID1A. Therefore, along with transcriptional repression, ARID1A-governed chromatin dynamics appear to influence DNA repair on the sex chromosomes.

Table 1. The loss of ARID1A results in a pachytene arrest.
Table outlining the distribution of P23 *Arid1a*^{WT} and *Arid1a*^{cKO} meiotic prophase-I profiles. SYCP3 staining determined meiotic staging. Co-staining of ARID1A identified mutant spermatocytes from escaper. The total number of spermatocytes scored included 166 for *Arida*$^{fl/fl}$ and 124 for *Arid1a*^{cKO}. * denotes *Arid1a*^{cKO} diplotene spermatocytes with partially reduced but not complete loss of ARID1A signal relative to controls.

Fig S1. ARID1A transcripts detected in pachytene spermatocytes.
scRNA-seq profiles of *Arid1a* and *Arid1b* in adult testes from B6 mice (Ernst et al., 2019). (A) tSNE plot describing the clustering of various spermatogenic stages. LOG2 normalized expression counts of (B,C) *Arid1a* and (D,E) *Arid1b* represented by tSNE plots and bar plots.

(B,D) tSNE plots illustrating the first (tSNE1, x-axis) and second dimensions (tSNE2, y-axis) . (C,E) Bar plots describe the gene's mRNA abundance (y-axis) across identified germ cell clusters (x-axis). (A) eP: early pachynema, mP: mid pachynema, lP: late pachynema, MI: Metaphase-I, MII: Metaphase-II, S1-S11: Spermatid stages. Plots generated with shiny app (https://marionilab.cruk.cam.ac.uk/SpermatoShiny)

Fig S2. Western blot for ARID1A in wild-type and mutant pachytene spermatocytes (left) and with quantitation (right). (B). Bars represent mean ± S.E.M. *; p<0.01.

Fig S3. Spermatogenesis appears unperturbed in *Arid1a^{cKO}* males.
Histological examination of (A) PAS-stained seminiferous tubule sections and (B) H&E-stained cauda epididymal sections obtained from 10-week-old *Arid1a^{WT} and Arid1a^{cKO}* mice. The micrograph depicts seminiferous tubule staging and scale bars (50 µm). Magnification: 40x.

Fig S4. *Arid1a^{cKO}* testes display inefficient *Stra8-Cre* activity.
(A) Schematic (top) illustrating the region of *Arid1a^{fl}* allele spanning exons (ex) 4-8 (grey boxes) along with the location of *loxP* sites (solid magenta arrowheads) and primer annealing sites (blue arrows). (A bottom): analysis of the RT-PCR of *Arid1a* transcripts from STA-PUT purified populations of *Arid1a^{WT} and Arid1a^{cKO}* pachytene spermatocytes (left) and round spermatids (right). DNA electrophoresis gels indicate bands corresponding to the fl: floxed and Δ: excised PCR products. *Arid1a^{WT}* and *Arid1a^{cKO}* (B) testes cryosections and (C) spermatocyte spreads, immunolabelled for ARID1A (magenta), SYCP3 (green), and counterstained for DNA (blue). (B) Scale bar: 20 µm, magnification: 63x, P: Pachytene, D: Diplotene, and M-I: Metaphase-I spermatocytes. (C) Scale bar:15 µm, magnification: 100x. Brightness of the whole panels (B,C) were increased by compressing the dynamic range of the image panels using Adobe photoshop (0-1-255 to 0-1-150).

Fig S5. Transcription start sites of differentially expressed autosomal and sex-linked genes display ARID1A occupancy.
(A-B) Heatmap (bottom) and metaplot (top) displaying the average gene-wide enrichment of ARID1A associated with differentially expressed (A) autosomal and (B) sex-linked genes in *Arid1a^{WT}* and *Arid1a^{cKO}* pachytene spermatocytes. (A-B) The number of RefSeq annotations (n) associated with differentially regulated autosomal and sex-linked genes (rows) is indicated. Up-reg: misexpressed and Dn-reg: misrepressed genes in response to the loss of ARID1A.

Average ARID1A CUT&RUN coverage was determined using two antibodies (anti-ARID1A^{Sigma}; anti-ARID1A^{CST}) plotted across RefSeq genes ± 3Kb.

Fig S6. ARID1A does not influence sex body formation.

(A) *Arid1a*^{WT} and *Arid1a*^{cKO} spermatocyte spreads immunolabelled for ARID1A (magenta) and γH2Ax (green). Scale bar:15 µm, magnification: 100x. (B) Cross section of adult (3-month-old) *Arid1a*^{WT} and *Arid1a*^{cKO} seminiferous tubules immunolabelled for ARID1A (green) and ATR (cyan). Scale bar:15 µm, magnification: 63x. (C) *Arid1a*^{WT} and *Arid1a*^{cKO} pachytene spermatocytes immunolabelled for MDC1 (magenta), SYCP3 (cyan), and ARID1A (green). Scale bar:15 µm, magnification: 100x. (A-B) DNA counterstained with DAPI (blue). Brightness of the whole image panel (C) was increased by compressing the dynamic range of the image panel using Adobe photoshop (0-1-255 to 0-1-150).

Fig S7. ARID1A does not influence the expression or incorporation of H3.3.

(A) Western blots on acid-extracted histones obtained from four independent replicates of P19 *Arid1a*^{WT} and *Arid1a*^{cKO} spermatogenic cells, displaying H3.3 abundance. Total histone levels from each sample are displayed. (B) *Arid1a*^{WT} and *Arid1a*^{cKO} pachytene spermatocytes immunolabelled for HORMAD1 (magenta), DAXX (cyan), and ARID1A (green). DNA counterstained with DAPI (blue). The sex chromosomes (yellow arrow) and sex body (yellow dashed circle) are labeled. Scale bar:15 µm, magnification: 100x. (C) *Arid1a*^{WT} and *Arid1a*^{cKO} testis cryosections immunolabelled for ARID1A (magenta) and HIRA (green). DNA counterstained with DAPI (blue). Representative mutant (white arrows) and escaper (yellow arrows) pachytene spermatocytes labeled in *Arid1a*^{cKO} testis cryosection. Scale bar: 15 µm, magnification: 63x. Brightness of the whole panels (B,C) were increased by compressing the dynamic range of the image panels using Adobe photoshop (0-1-255 to 0-1-150).

Fig S8. ARID1A limits H3.3 occupancy at promoters

(A) Genomic associations of MACS2 H3.3 peak calls from *Arid1a*^{WT} and *Arid1a*^{cKO} pachytene spermatocytes. Percent (%) distribution of genomic annotations is indicated. (B-C) Heatmap (bottom) and metaplot (top) displaying the average H3.3 signal associated with differentially expressed (B) autosomal and (C) sex-linked genes in *Arid1a*^{WT} and *Arid1a*^{cKO} pachytene spermatocytes. (B-C) The number of RefSeq annotations (n) associated with differentially regulated genes (rows) is indicated. Up-reg: misexpressed, and Dn-reg: misrepressed genes in response to the loss of ARID1A. Average H3.3 coverage plotted across RefSeq genes ± 3Kb.

Fig S9. Genome browser views of ARID1A governed H3.3 genomic associations.
H3.3 CUT&RUN coverage from *Arid1a*^{WT} (green tracks) and *Arid1a*^{cKO} (Orange tracks) pachytene spermatocytes. Solid red bars and yellow highlights denote H3.3 peak calls (MACS2) from *Arid1a*^{WT} and *Arid1a*^{cKO} pachytene spermatocytes. Vertical viewing limits within parentheses.

Fig S10. H3.3 occupancy is antagonistic to DMC1 associations in non-homologous sex-linked regions.
(A) Genomic associations of common (C1-C4) and gained (G1-G4) k-means clusters in pachytene spermatocytes. Percent (%) distribution of genomic annotations is indicated. (B) Results of PRDM9 motif enrichment analyses at gained (G1 and G3), k-means clusters (top), and plots describing the frequency of PRDM9 motifs (y-axis) spanning a 5 Kb window centered at ATAC-seq peaks (x-axis) associated with gained (middle) and common (bottom) k-means clusters that are either deficient (orange trend line) or enriched (cyan trend line) for H3.3 occupancy. Trend lines were generated using generalized additive mode smoothing (gam). 95% confidence interval (gray shading) is indicated. (C-D) Heatmaps displaying testes DMC1 (left) and pachytene spermatocyte associated H3K4me3 (right) enrichment relative to input at k-means clusters associated with (C) gained (G1-G4), and (D) common (C1-C4) ATAC-seq peaks. (C-D) DMC1 and H3K4me3 coverage plotted over a 10 Kb window centered at ATAC-seq peaks (MACS2).

Fig S11. ARID1A does not affect the axial association of RAD51 with the XY during pachynema.
(A) Heatmaps displaying testes RAD51 enrichment relative to input at k-means clusters associated with gained (G1-G4, left) and common (C1-C4, right) ATAC-seq peaks. RAD51 coverage plotted over a 10 Kb window centered at ATAC-seq peaks (MACS2). (B) *Arid1a*^{WT} and *Arid1a*^{cKO} pachytene spermatocytes immunolabelled for HORMAD1 (magenta), RAD51 (green) and counterstained with DAPI (blue). Scale bar:15 µm, magnification: 100x. Yellow arrows and dashed circles label the sex chromosomes.

Table S1. There is no significant difference in the numbers of undifferentiated spermatogonia expressing PLZF in 1-month-old *Arid1a*^{cKO} relative to *Arid1a*$^{fl/fl}$ males.

References

Ahmed, E. A. and de Rooij, D. G. (2009). Staging of Mouse Seminiferous Tubule Cross-Sections. In *Meiosis* (ed. Keeney, S.), pp. 263–277. Totowa, NJ: Humana Press.

Alavattam, K. G., Maezawa, S., Andreassen, P. R. and Namekawa, S. H. (2022). Meiotic sex chromosome inactivation and the XY body: a phase separation hypothesis. *Cell. Mol. Life Sci.* **79**, 18.

Alexander, A. K., Rice, E. J., Barshad, G., Zhu, L., Cohen, P. E. and Danko, C. G. (2022). Meiotic gene transcription programs are mediated by A-MYB and BRDT-dependent RNA polymerase II pause release during mammalian prophase I. *bioRxiv*, doi.org/10.1101/2022.08.19.504615.

Amemiya, H. M., Kundaje, A. and Boyle, A. P. (2019). The ENCODE Blacklist: Identification of Problematic Regions of the Genome. *Scientific Reports* **9**, 9354.

Baarends, W. M., Wassenaar, E., van der Laan, R., Hoogerbrugge, J., Sleddens-Linkels, E., Hoeijmakers, J. H. J., de Boer, P. and Grootegoed, J. A. (2005). Silencing of Unpaired Chromatin and Histone H2A Ubiquitination in Mammalian Meiosis. *Molecular and Cellular Biology* **25**, 1041–1053.

Bellvé, A. R. (1993). [6] Purification, culture, and fractionation of spermatogenic cells. In *Methods in Enzymology*, **225**, pp. 84–113.

Bioconductor Core Team (2019). TxDb.Mmusculus.UCSC.mm10.knownGene: Annotation package for TxDb object(s).

Brick, K., Smagulova, F., Khil, P., Camerini-Otero, R. D. and Petukhova, G. V. (2012). Genetic recombination is directed away from functional genomic elements in mice. *Nature* **485**, 642–645.

Chakraborty, P. and Magnuson, T. (2022). INO80 requires a polycomb subunit to regulate the establishment of poised chromatin in murine spermatocytes. *Development* **149**, dev200089.

Chandler, R. L., Damrauer, J. S., Raab, J. R., Schisler, J. C., Wilkerson, M. D., Didion, J. P., Starmer, J., Serber, D., Yee, D., Xiong, J., et al. (2015). Coexistent ARID1A–PIK3CA mutations promote ovarian clear-cell tumorigenesis through pro-tumorigenic inflammatory cytokine signalling. *Nature Communications* **6**, 6118.

Chaumeil, J., Le Baccon, P., Wutz, A. and Heard, E. (2006). A novel role for Xist RNA in the formation of a repressive nuclear compartment into which genes are recruited when silenced. *Genes and Development* **20**, 2223–2237.

Clapier, C. R., Iwasa, J., Cairns, B. R. and Peterson, C. L. (2017). Mechanisms of action and regulation of ATP-dependent chromatin-remodelling complexes. *Nature Reviews Molecular Cell Biology* **18**, 407-422.

Corces, M. R., Trevino, A. E., Hamilton, E. G., Greenside, P. G., Sinnott-Armstrong, N. A., Vesuna, S., Satpathy, A. T., Rubin, A. J., Montine, K. S., Wu, B., et al. (2017). An

improved ATAC-seq protocol reduces background and enables interrogation of frozen tissues. *Nat Methods* **14**, 959–962.

Ellnati, E., Russell, H. R., Ojarikre, O. A., Sangrithi, M., Hirota, T., de Rooij, D. G., McKinnon, P. J. and Turner, J. M. A. (2017). DNA damage response protein TOPBP1 regulates X chromosome silencing in the mammalian germ line. *Proc. Natl. Acad. Sci. U.S.A.* **114**, 12536–12541.

Ernst, C., Eling, N., Martinez-Jimenez, C. P., Marioni, J. C. and Odom, D. T. (2019). Staged developmental mapping and X chromosome transcriptional dynamics during mouse spermatogenesis. *Nat Commun* **10**, 1251.

Fernandez-Capetillo, O., Mahadevaiah, S. K., Celeste, A., Romanienko, P. J., Camerini-Otero, R. D., Bonner, W. M., Manova, K., Burgoyne, P. and Nussenzweig, A. (2003). H2AX Is Required for Chromatin Remodeling and Inactivation of Sex Chromosomes in Male Mouse Meiosis. *Developmental Cell* **4**, 497–508.

Fontaine, E., Papin, C., Martinez, G., Le Gras, S., Nahed, R. A., Héry, P., Buchou, T., Ouararhni, K., Favier, B., Gautier, T., et al. (2022). Dual role of histone variant H3.3B in spermatogenesis: positive regulation of piRNA transcription and implication in X-chromosome inactivation. *Nucleic Acids Res* **50**, 7350–7366.

Gray, S., Santiago, E. R., Chappie, J. S. and Cohen, P. E. (2020). Cyclin N-Terminal Domain-Containing-1 Coordinates Meiotic Crossover Formation with Cell-Cycle Progression in a Cyclin-Independent Manner. *Cell Rep* **32**, 107858.

Handel, M. (2004). The XY body: a specialized meiotic chromatin domain. *Experimental Cell Research* **296**, 57–63.

Hasegawa, K., Sin, H.-S., Maezawa, S., Broering, T. J., Kartashov, A. V., Alavattam, K. G., Ichijima, Y., Zhang, F., Bacon, W. C., Greis, K. D., et al. (2015). SCML2 establishes the male germline epigenome through regulation of histone H2A ubiquitination. *Dev. Cell* **32**, 574–588.

Hinch, A. G., Becker, P. W., Li, T., Moralli, D., Zhang, G., Bycroft, C., Green, C., Keeney, S., Shi, Q., Davies, B., et al. (2020). The Configuration of RPA, RAD51, and DMC1 Binding in Meiosis Reveals the Nature of Critical Recombination Intermediates. *Molecular Cell* **79**, 689-701.e10.

Hirota, T., Blakeley, P., Sangrithi, M. N., Mahadevaiah, S. K., Encheva, V., Snijders, A. P., Ellnati, E., Ojarikre, O. A., de Rooij, D. G., Niakan, K. K., et al. (2018). SETDB1 Links the Meiotic DNA Damage Response to Sex Chromosome Silencing in Mice. *Developmental Cell* **47**, 645-659.e6.

Ichijima, Y., Ichijima, M., Lou, Z., Nussenzweig, A., Camerini-Otero, R. D., Chen, J., Andreassen, P. R. and Namekawa, S. H. (2011). MDC1 directs chromosome-wide silencing of the sex chromosomes in male germ cells. *Genes Dev.* **25**, 959–971.

Keniry, A., Jansz, N., Gearing, L. J., Wanigasuriya, I., Chen, J., Nefzger, C. M., Hickey, P. F., Gouil, Q., Liu, J., Breslin, K. A., et al. (2022). BAF complex-mediated chromatin

relaxation is required for establishment of X chromosome inactivation. *Nature Communications* **13**, 1658.

Khalil, A. M., Boyar, F. Z. and Driscoll, D. J. (2004). Dynamic histone modifications mark sex chromosome inactivation and reactivation during mammalian spermatogenesis. *Proc Natl Acad Sci U S A* **101**, 16583–16587.

Kim, Y., Fedoriw, A. M. and Magnuson, T. (2012). An essential role for a mammalian SWI/SNF chromatin-remodeling complex during male meiosis. *Development* **139**, 1133–1140.

Langmead, B. and Salzberg, S. L. (2012). Fast gapped-read alignment with Bowtie 2. *Nature Methods* **9**, 357–359.

Li, H., Handsaker, B., Wysoker, A., Fennell, T., Ruan, J., Homer, N., Marth, G., Abecasis, G. and Durbin, R. (2009). The Sequence Alignment/Map format and SAMtools. *Bioinformatics* **25**, 2078–2079.

Love, M. I., Huber, W. and Anders, S. (2014). Moderated estimation of fold change and dispersion for RNA-seq data with DESeq2. *Genome Biol* **15**, 550.

Lun, A. T. L. and Smyth, G. K. (2015). Csaw: A Bioconductor package for differential binding analysis of ChIP-seq data using sliding windows. *Nucleic Acids Research* **44**, 1–10.

Maezawa, S., Hasegawa, K., Yukawa, M., Kubo, N., Sakashita, A., Alavattam, K. G., Sin, H.-S., Kartashov, A. V., Sasaki, H., Barski, A., et al. (2018a). Polycomb protein SCML2 facilitates H3K27me3 to establish bivalent domains in the male germline. *Proc. Natl. Acad. Sci. U.S.A.* **115**, 4957–4962.

Maezawa, S., Yukawa, M., Alavattam, K. G., Barski, A. and Namekawa, S. H. (2018b). Dynamic reorganization of open chromatin underlies diverse transcriptomes during spermatogenesis. *Nucleic Acids Research* **46**, 593–608.

Manterola, M., Brown, T. M., Oh, M. Y., Garyn, C., Gonzalez, B. J. and Wolgemuth, D. J. (2018). BRDT is an essential epigenetic regulator for proper chromatin organization, silencing of sex chromosomes and crossover formation in male meiosis. *PLoS Genet* **14**, e1007209.

Meers, M. P., Bryson, T. D., Henikoff, J. G. and Henikoff, S. (2019). Improved CUT&RUN chromatin profiling tools. *eLife* **8**, e46314.

Meistrich, M. L. and Hess, R. A. (2013). Assessment of Spermatogenesis Through Staging of Seminiferous Tubules. In *Spermatogenesis* (ed. Carrell, D. T.) and Aston, K. I.), pp. 299–307. Totowa, NJ: Humana Press.

Menon, D. U., Shibata, Y., Mu, W. and Magnuson, T. (2019). Mammalian SWI/SNF collaborates with a polycomb-associated protein to regulate male germ line transcription in the mouse. *Development* **146,** dev.174094

Menon, D. U., Kirsanov, O., Geyer, C. B. and Magnuson, T. (2021). Mammalian SWI/SNF chromatin remodeler is essential for reductional meiosis in males. *Nat Commun* **12**, 6581.

Moens, P. B., Chen, D. J., Shen, Z., Kolas, N., Tarsounas, M., Heng, H. H. Q. and Spyropoulos, B. (1997). Rad51 immunocytology in rat and mouse spermatocytes and oocytes. *Chromosoma* **106**, 207–215.

Moens, P. B., Kolas, N. K., Tarsounas, M., Marcon, E., Cohen, P. E. and Spyropoulos, B. (2002). The time course and chromosomal localization of recombination-related proteins at meiosis in the mouse are compatible with models that can resolve the early DNA-DNA interactions without reciprocal recombination. *J Cell Sci* **115**, 1611–1622.

Monesi, V. (1964). Ribonucleic acid synthesis during mitosis and meiosis in the mouse testis. *Journal of Cell Biology* **22**, 521–532.

Noe Gonzalez, M., Blears, D. and Svejstrup, J. Q. (2021). Causes and consequences of RNA polymerase II stalling during transcript elongation. *Nat Rev Mol Cell Biol* **22**, 3–21.

O'Brien, D. (1993). Isolation, separation, and short-term culture of spermatogenic cells. In *Methods in Toxicology*, pp. 246–264. San Diego: Academic Press.

Pàges, H., Carlson, M., Falcon, S. and Nianhua, L. (2021). AnnotationDbi: Manipulation of SQLite-based annotations in Bioconductor. *R package version 1.562.2*.

Patro, R., Duggal, G., Love, M. I., Irizarry, R. A. and Kingsford, C. (2017). Salmon provides fast and bias-aware quantification of transcript expression. *Nat Methods* **14**, 417–419.

Quinlan, A. R. and Hall, I. M. (2010). BEDTools: A flexible suite of utilities for comparing genomic features. *Bioinformatics* **26**, 841–842.

Ramírez, F., Ryan, D. P., Grüning, B., Bhardwaj, V., Kilpert, F., Richter, A. S., Heyne, S., Dündar, F. and Manke, T. (2016). deepTools2: a next generation web server for deep-sequencing data analysis. *Nucleic Acids Res* **44**, W160–W165.

Reske, J. J., Wilson, M. R., Armistead, B., Harkins, S., Perez, C., Hrit, J., Adams, M., Rothbart, S. B., Missmer, S. A., Fazleabas, A. T., et al. (2022). ARID1A-dependent maintenance of H3.3 is required for repressive CHD4-ZMYND8 chromatin interactions at super-enhancers. *BMC Biology* **20**, 209.

Robinson, J. T., Thorvaldsdóttir, H., Winckler, W., Guttman, M., Lander, E. S., Getz, G. and Mesirov, J. P. (2011). Integrative genomics viewer. *Nat Biotechnol* **29**, 24–26.

Rogers, R. S., Inselman, A., Handel, M. A. and Matunis, M. J. (2004). SUMO modified proteins localize to the XY body of pachytene spermatocytes. *Chromosoma* **113**, 233–243.

Royo, H., Prosser, H., Ruzankina, Y., Mahadevaiah, S. K., Cloutier, J. M., Baumann, M., Fukuda, T., Höög, C., Tóth, A., de Rooij, D. G., et al. (2013). ATR acts stage specifically to regulate multiple aspects of mammalian meiotic silencing. *Genes Dev.* **27**, 1484–1494.

Sadate-Ngatchou, P. I., Payne, C. J., Dearth, A. T. and Braun, R. E. (2008). Cre recombinase activity specific to postnatal, premeiotic male germ cells in transgenic mice. *Genesis* **46**, 738–742.

Schimenti, J. (2005). Synapsis or silence. *Nat Genet* **37**, 11–13.

Schindelin, J., Arganda-Carreras, I., Frise, E., Kaynig, V., Longair, M., Pietzsch, T., Preibisch, S., Rueden, C., Saalfeld, S., Schmid, B., et al. (2012). Fiji: An open-source platform for biological-image analysis. *Nature Methods* **9,** 676-682.

Shechter, D., Dormann, H. L., Allis, C. D. and Hake, S. B. (2007). Extraction, purification and analysis of histones. *Nature Protocols* **2**, 1445–1457.

Skene, P. J. and Henikoff, S. (2017). An efficient targeted nuclease strategy for high-resolution mapping of DNA binding sites. *eLife* **6**, e21856.

Soneson, C., Love, M. I. and Robinson, M. D. (2016). Differential analyses for RNA-seq: transcript-level estimates improve gene-level inferences. *F1000Research* **4**, 1521.

Turner, J. M. A. (2007). Meiotic sex chromosome inactivation. *Development* **134**, 1823–1831.

Turner, J. M. A., Aprelikova, O., Xu, X., Wang, R., Kim, S., Chandramouli, G. V. R., Barrett, J. C., Burgoyne, P. S. and Deng, C.-X. (2004). BRCA1, Histone H2AX Phosphorylation, and Male Meiotic Sex Chromosome Inactivation. *Current Biology* **14**, 2135–2142.

Turner, J. M. A., Mahadevaiah, S. K., Fernandez-Capetillo, O., Nussenzweig, A., Xu, X., Deng, C.-X. and Burgoyne, P. S. (2005). Silencing of unsynapsed meiotic chromosomes in the mouse. *Nat Genet* **37**, 41–47.

van der Heijden, G. W., Derijck, A. A. H. A., Pósfai, E., Giele, M., Pelczar, P., Ramos, L., Wansink, D. G., van der Vlag, J., Peters, A. H. F. M. and de Boer, P. (2007). Chromosome-wide nucleosome replacement and H3.3 incorporation during mammalian meiotic sex chromosome inactivation. *Nat Genet* **39**, 251–258.

Wang, J., Gu, H., Lin, H. and Chi, T. (2012). Essential roles of the chromatin remodeling factor BRG1 in spermatogenesis in mice. *Biol. Reprod.* **86**, 186.

Wen, H., Li, Y., Xi, Y., Jiang, S., Stratton, S., Peng, D., Tanaka, K., Ren, Y., Xia, Z., Wu, J., et al. (2014). ZMYND11 links histone H3.3K36me3 to transcription elongation and tumour suppression. *Nature* **508**, 263–268.

Yuen, B. T. K., Bush, K. M., Barrilleaux, B. L., Cotterman, R. and Knoepfler, P. S. (2014). Histone H3.3 regulates dynamic chromatin states during spermatogenesis. *Development* **141**, 3483–3494.

Zerbino, D. R., Johnson, N., Juettemann, T., Wilder, S. P. and Flicek, P. (2014). WiggleTools: Parallel processing of large collections of genome-wide datasets for visualization and statistical analysis. *Bioinformatics*. 30, 1008-1009.

Zhang, Y., Liu, T., Meyer, C. A., Eeckhoute, J., Johnson, D. S., Bernstein, B. E., Nussbaum, C., Myers, R. M., Brown, M., Li, W., et al. (2008). Model-based analysis of ChIP-Seq (MACS). *Genome Biology* **9**, R137

Meiotic Profile (P23)	*Arid1a*$^{fl/fl}$ (n= 166)	*Arid1a*^{cKO} (n= 124)
Pre-Lep/Leptonema	3.6 %	13.7 %
Zygonema	-	15.3 %
Early Pachynema	13.8 %	12.9 %
Mid Pachynema	22.89 %	40.3 %
late Pachynema	7.22 %	7.2 %
Early Diplonema	38.5 %	4.8 % *
Late Diplonema	14.45 %	5.6 % *

Table 1. The loss of ARID1A results in a pachytene arrest.

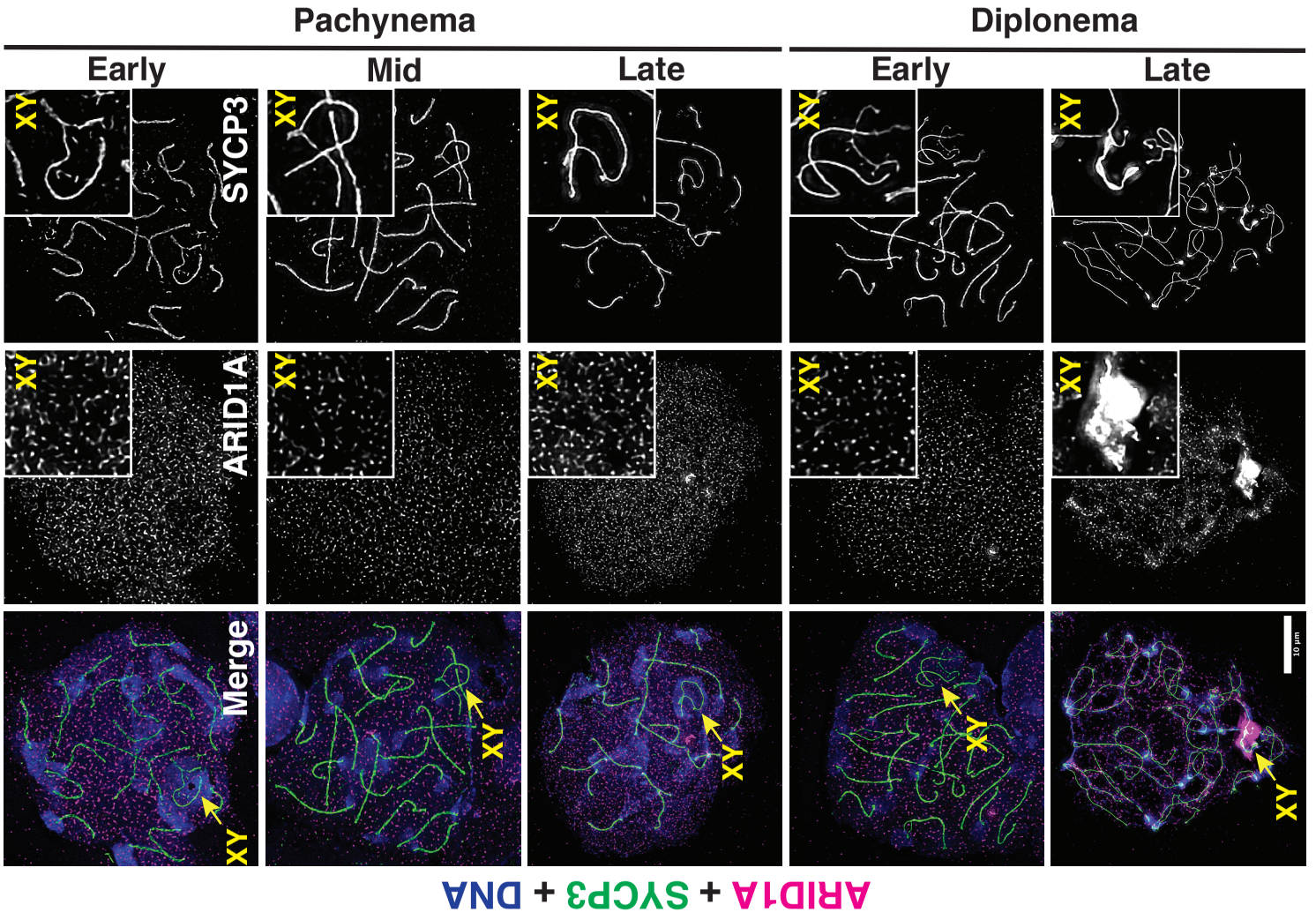
Pachynema
Diplonema
Early
Mid
Late
Early
Late
SYCP3
ARID1A
Merge
XY
10 µm
ARID1A + SYCP3 + DNA

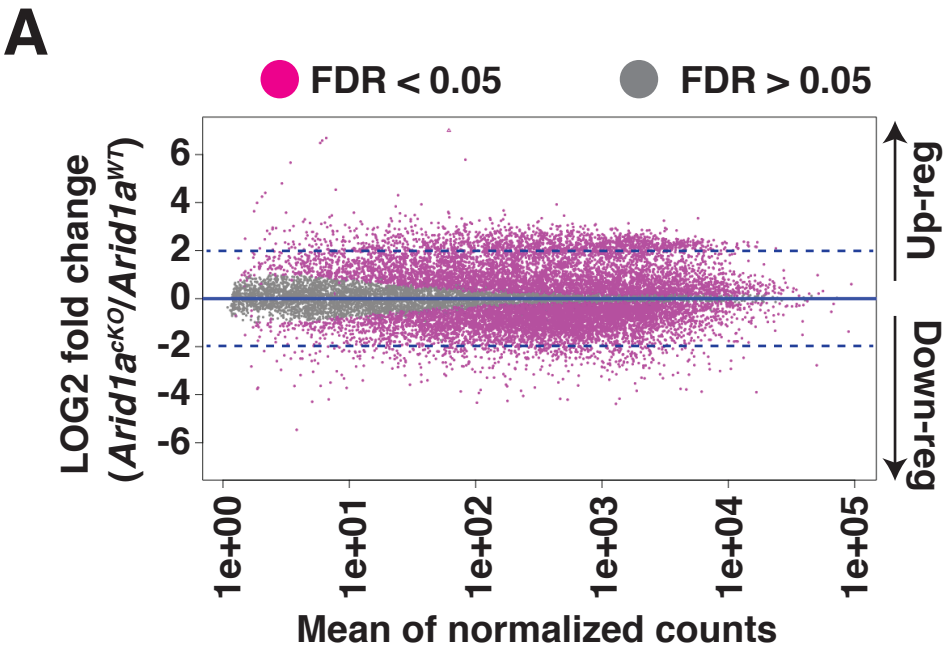
A
FDR < 0.05
FDR > 0.05
LOG2 fold change
(Arid1a^cKO/Arid1a^WT)
6
4
2
0
-2
-4
-6
Up-reg
Down-reg
1e+00
1e+01
1e+02
1e+03
1e+04
1e+05
Mean of normalized counts

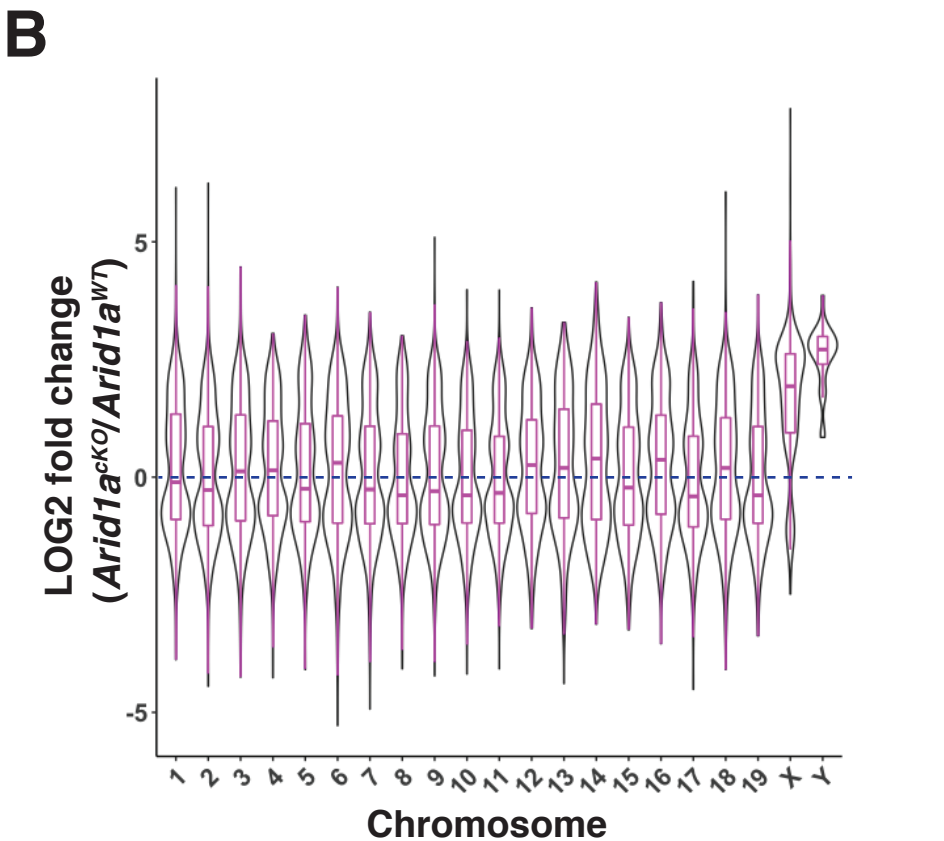
B
LOG2 fold change
(Arid1a^cKO/Arid1a^WT)
5
0
-5
1
2
3
4
5
6
7
8
9
10
11
12
13
14
15
16
17
18
19
X
Y
Chromosome

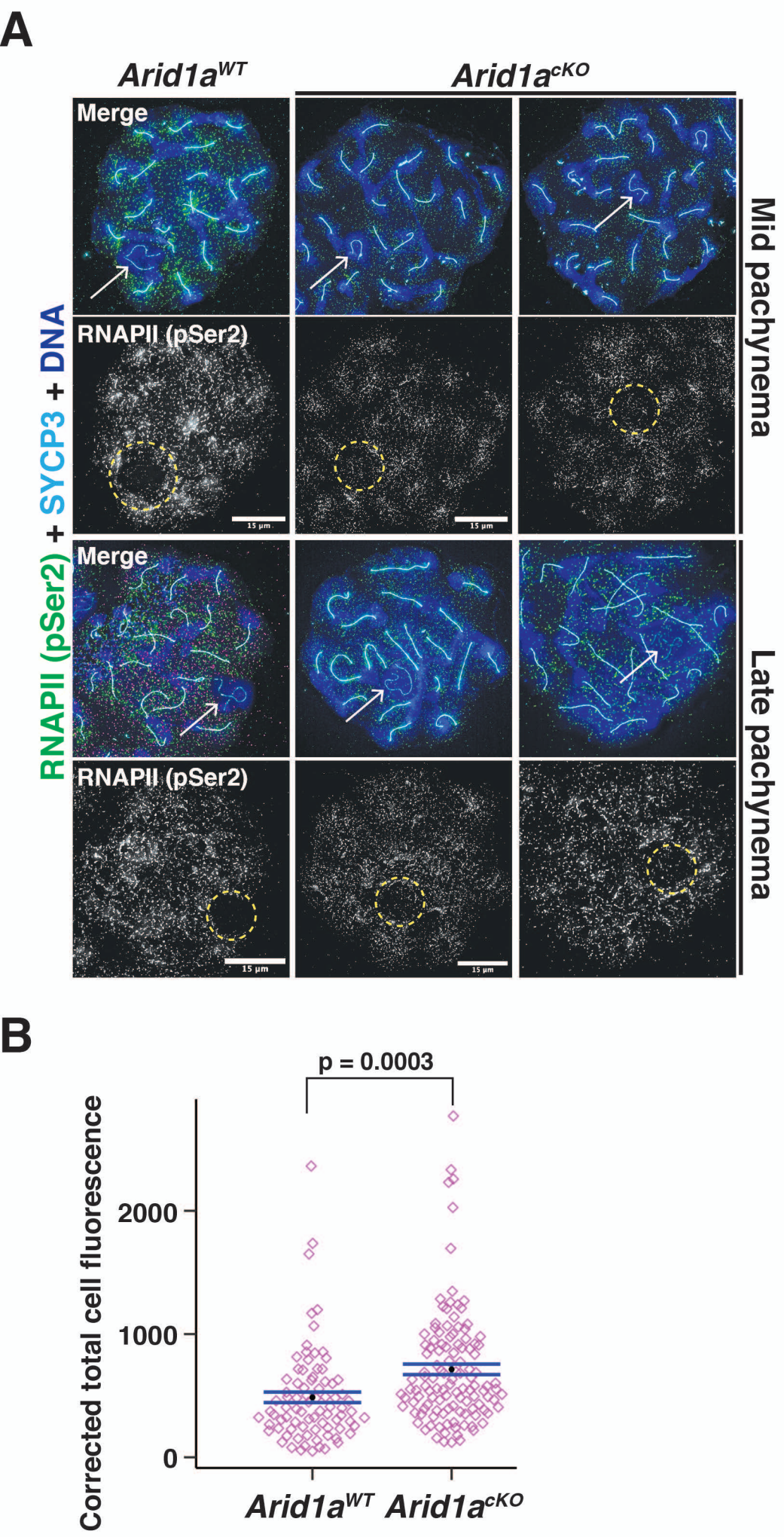
A
Arid1a^WT
Arid1a^cKO
Merge
RNAPII (pSer2)
RNAPII (pSer2) + SYCP3 + DNA
Mid pachynema
Late pachynema
15 µm
B
p = 0.0003
Corrected total cell fluorescence
2000
1000
0
Arid1a^WT
Arid1a^cKO

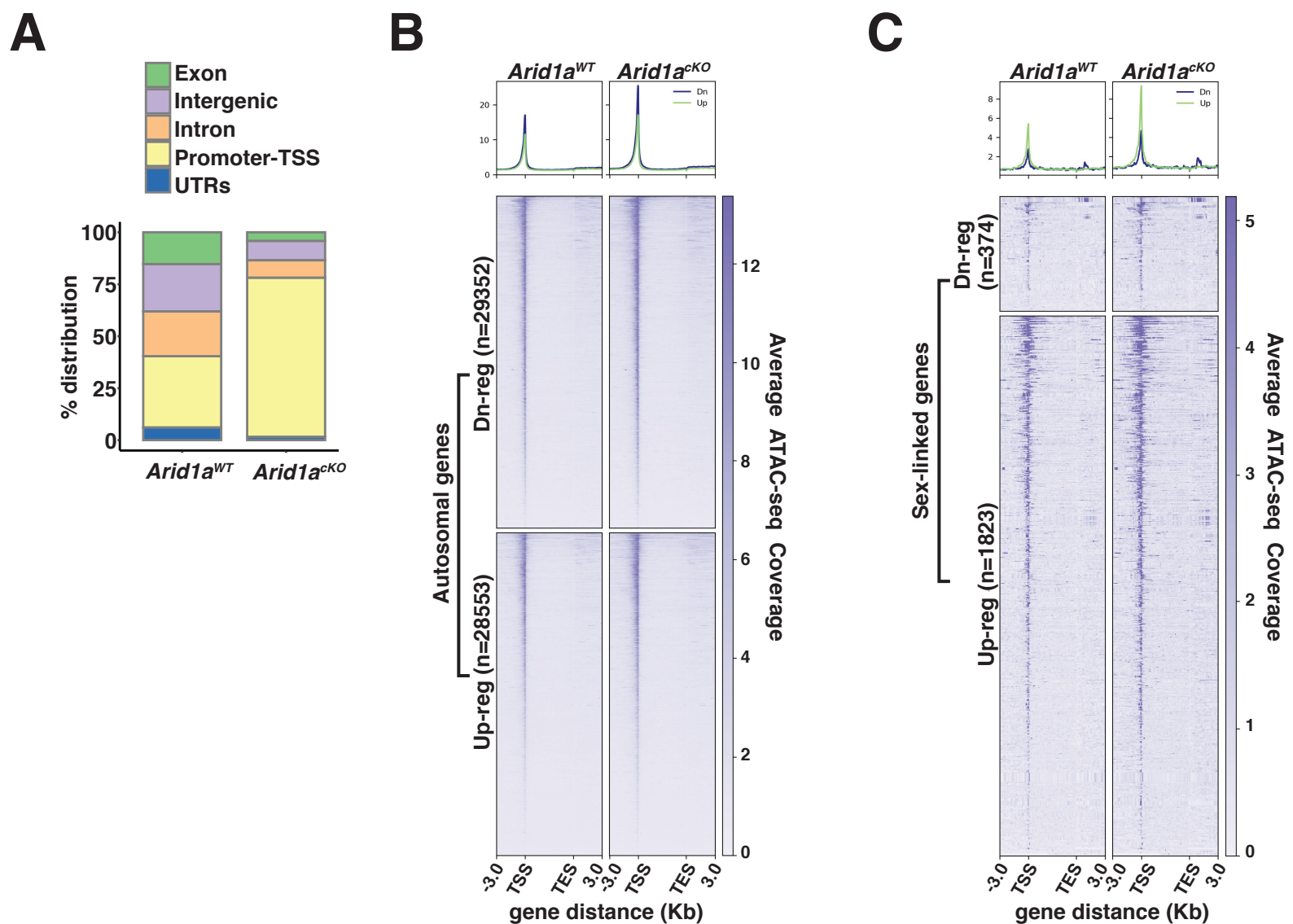
A
Exon
Intergenic
Intron
Promoter-TSS
UTRs
% distribution
100
75
50
25
0
Arid1a^WT
Arid1a^cKO
B
Arid1a^WT
Arid1a^cKO
Dn
Up
Autosomal genes
Dn-reg (n=29352)
Up-reg (n=28553)
Average ATAC-seq Coverage
-3.0
TSS
TES
3.0
gene distance (Kb)
C
Arid1a^WT
Arid1a^cKO
Dn
Up
Sex-linked genes
Dn-reg (n=374)
Up-reg (n=1823)
Average ATAC-seq Coverage
-3.0
TSS
TES
3.0
gene distance (Kb)

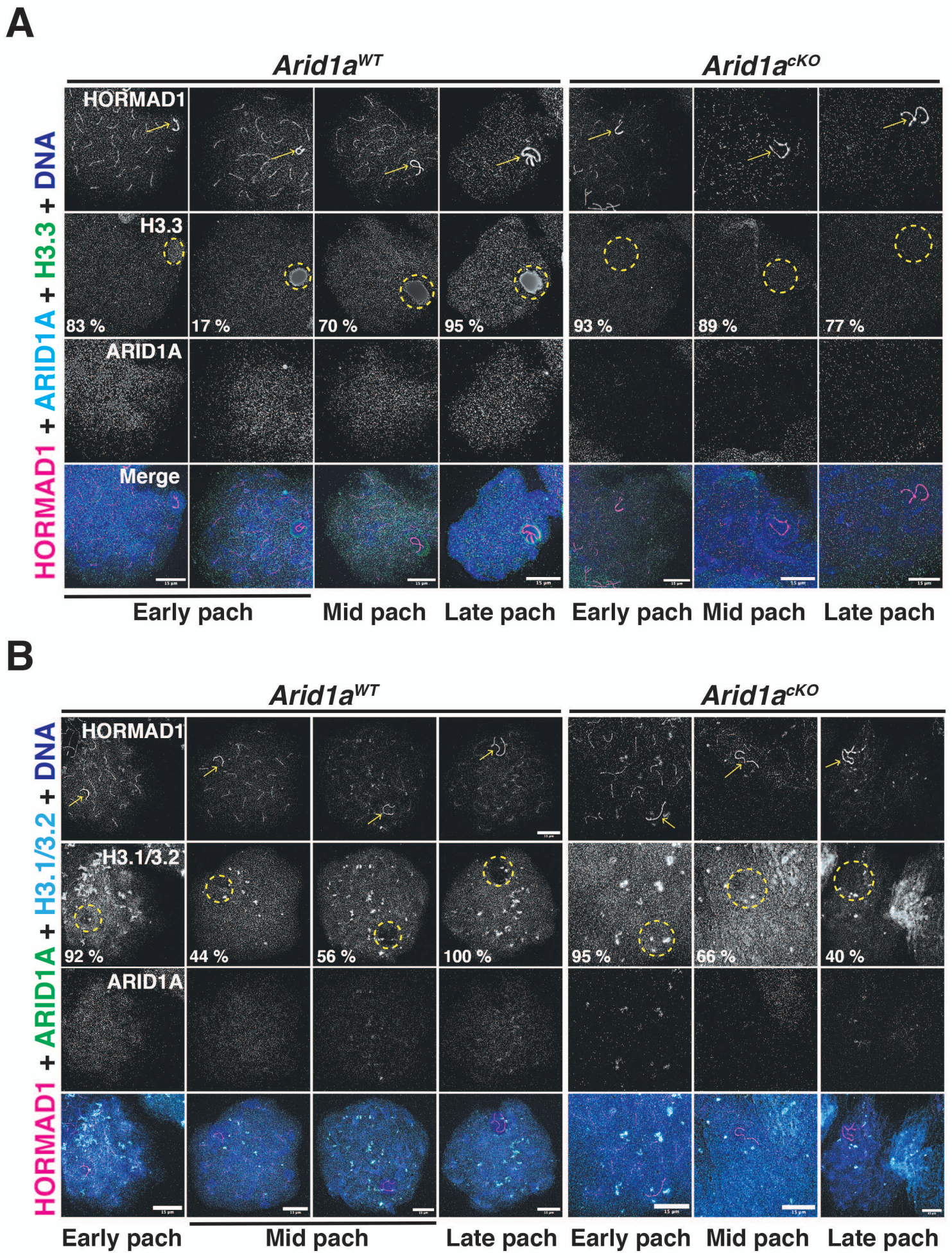
A
Arid1a^WT
Arid1a^cKO
HORMAD1 + ARID1A + H3.3 + DNA
HORMAD1
H3.3
ARID1A
Merge
83 %
17 %
70 %
95 %
93 %
89 %
77 %
Early pach
Mid pach
Late pach
Early pach
Mid pach
Late pach
B
Arid1a^WT
Arid1a^cKO
HORMAD1 + ARID1A + H3.1/3.2 + DNA
HORMAD1
H3.1/3.2
ARID1A
92 %
44 %
56 %
100 %
95 %
66 %
40 %
Early pach
Mid pach
Late pach
Early pach
Mid pach
Late pach

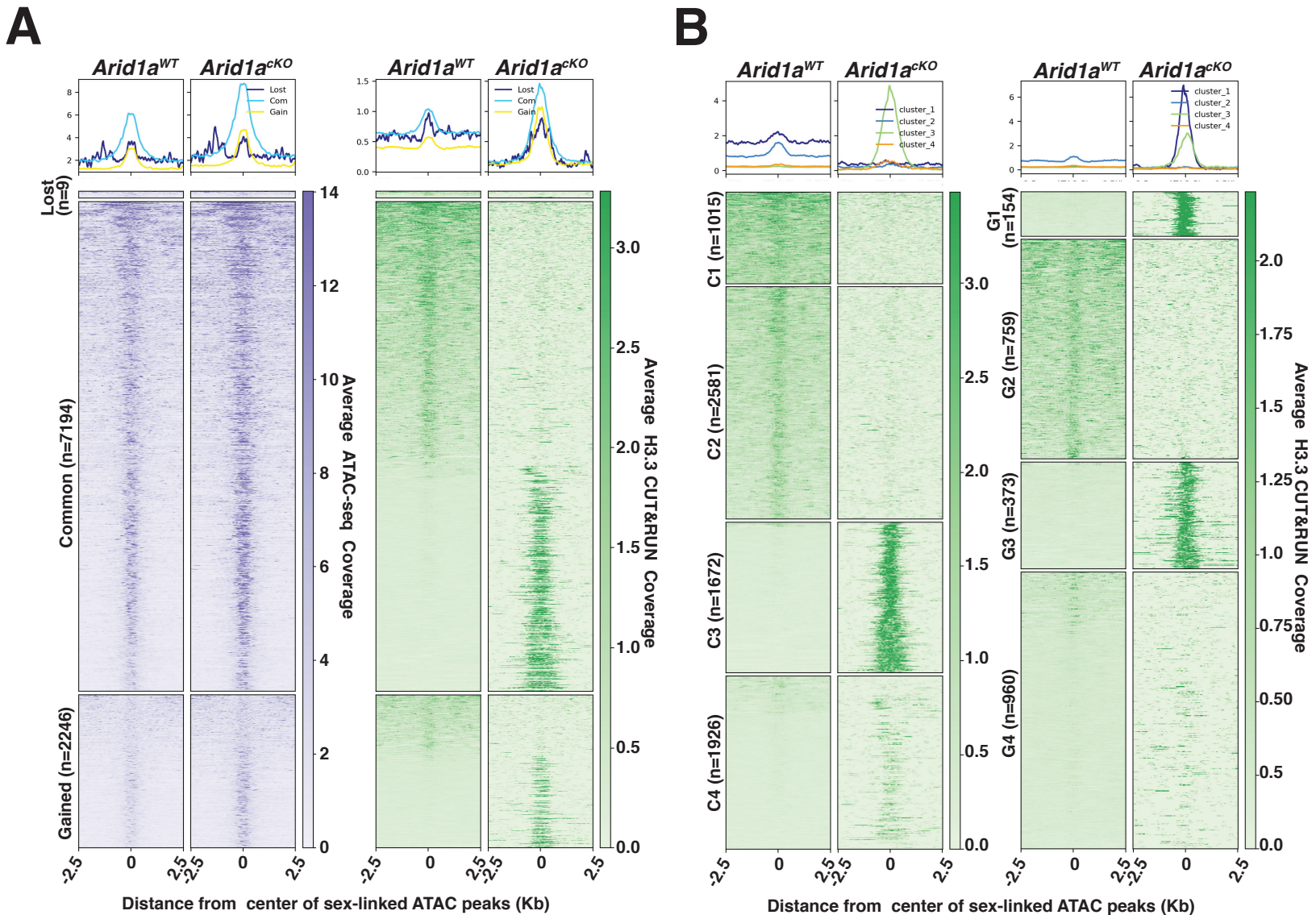
A
Arid1a^WT
Arid1a^cKO
Lost
Com
Gain
Lost (n=9)
Common (n=7194)
Gained (n=2246)
Average ATAC-seq Coverage
Average H3.3 CUT&RUN Coverage
Distance from center of sex-linked ATAC peaks (Kb)
B
cluster_1
cluster_2
cluster_3
cluster_4
C1 (n=1015)
C2 (n=2581)
C3 (n=1672)
C4 (n=1926)
G1 (n=154)
G2 (n=759)
G3 (n=373)
G4 (n=960)
Average H3.3 CUT&RUN Coverage
Distance from center of sex-linked ATAC peaks (Kb)

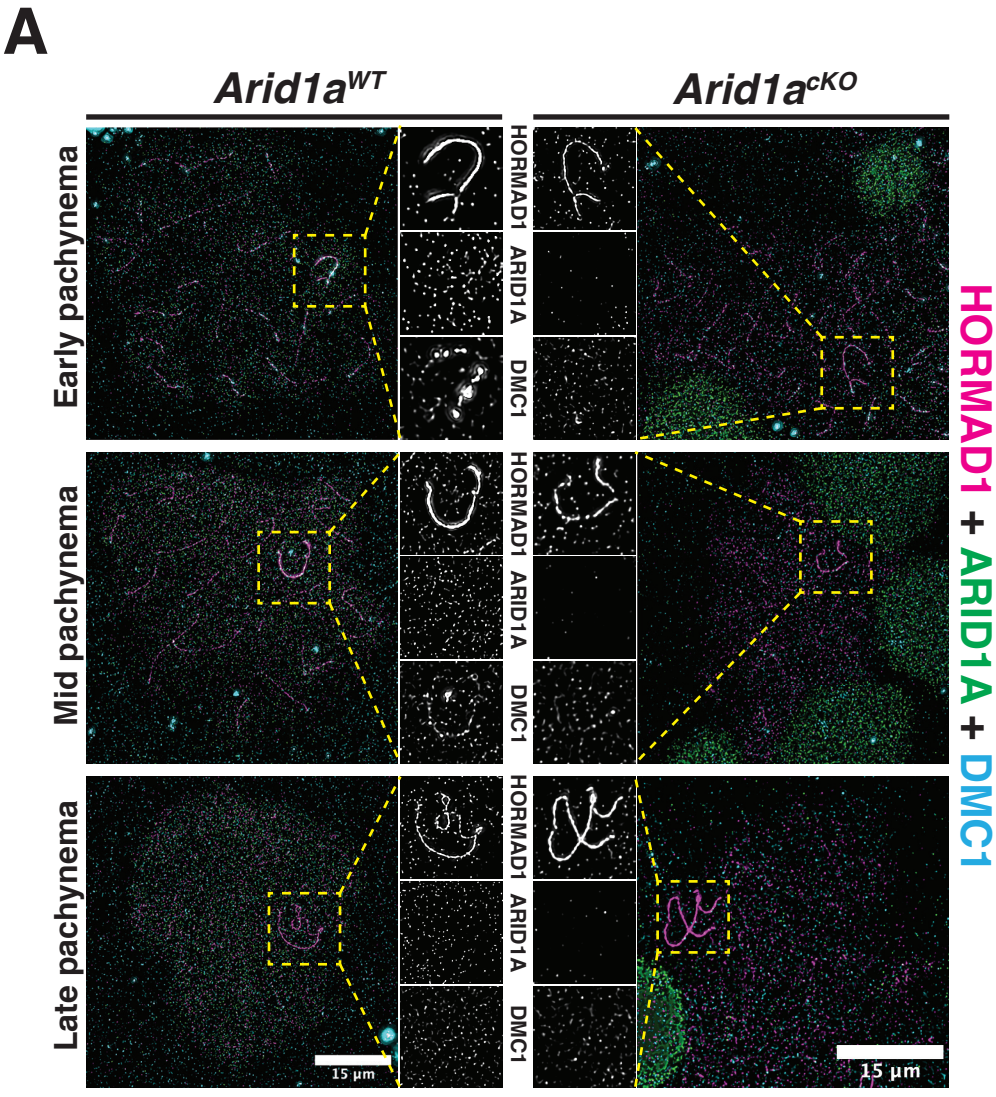
A
Arid1a^WT
Arid1a^cKO
Early pachynema
Mid pachynema
Late pachynema
HORMAD1
ARID1A
DMC1
HORMAD1 + ARID1A + DMC1
15 µm
15 µm

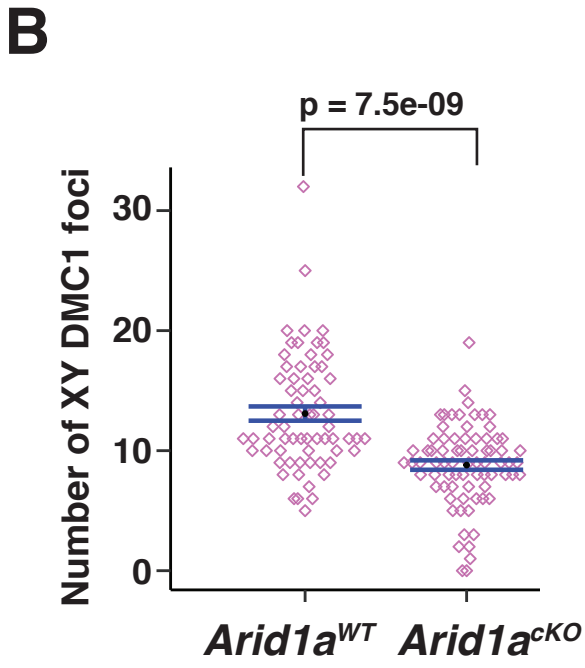
B
p = 7.5e-09
Number of XY DMC1 foci
30
20
10
0
Arid1a^WT
Arid1a^cKO

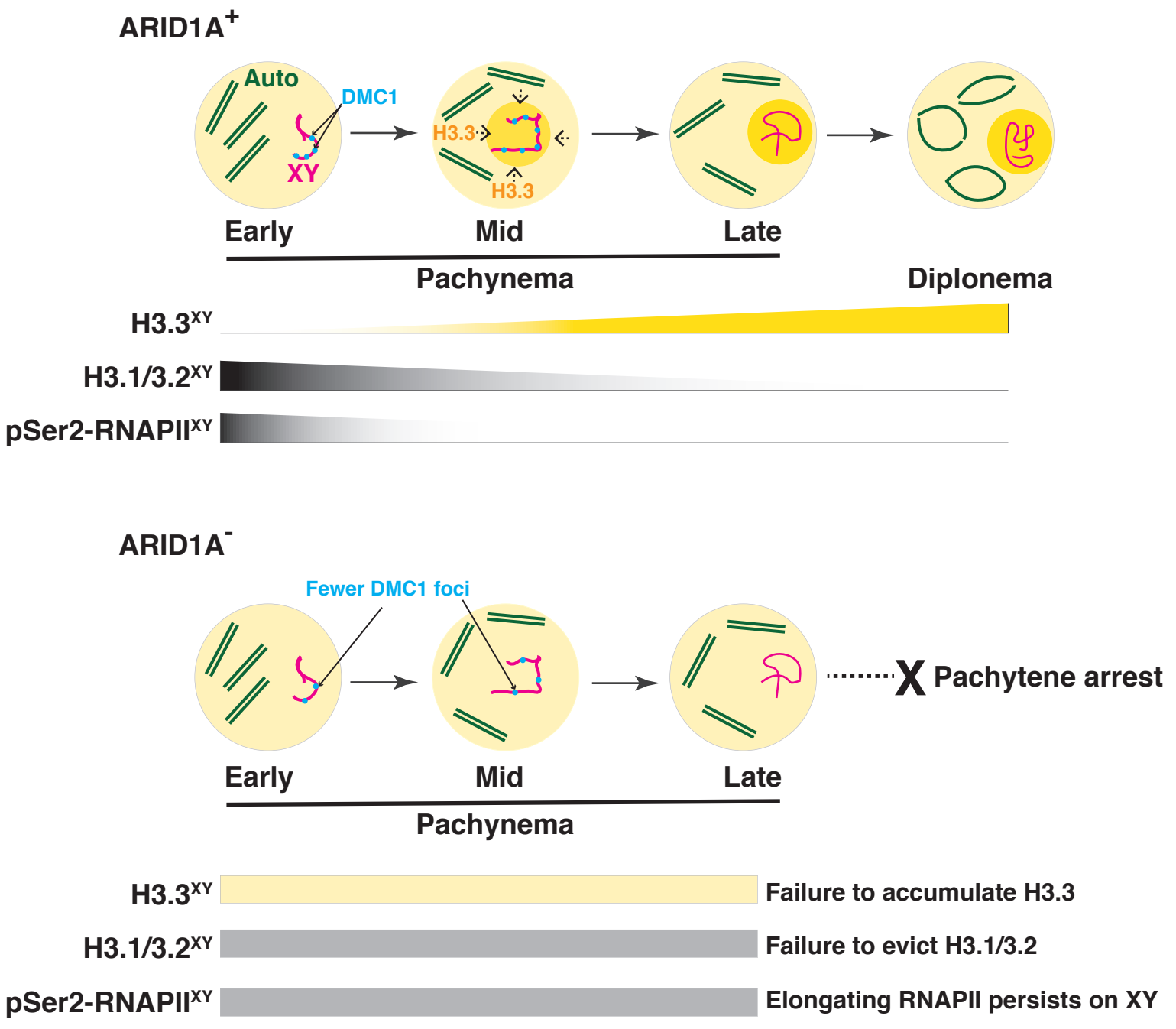
ARID1A+
Auto
DMC1
XY
H3.3
H3.3
Early
Mid
Late
Pachynema
Diplonema
H3.3XY
H3.1/3.2XY
pSer2-RNAPIIXY
ARID1A-
Fewer DMC1 foci
X Pachytene arrest
Early
Mid
Late
Pachynema
H3.3XY
Failure to accumulate H3.3
H3.1/3.2XY
Failure to evict H3.1/3.2
pSer2-RNAPIIXY
Elongating RNAPII persists on XY